Collective cell durotaxis emerges from long-range intercellular force transmission

Authors: Raimon Sunyer[1], Vito Conte[1], Jorge Escribano[2], Alberto Elosegui-Artola[1], Anna Labernadie[1], Leo Valon[1], Daniel Navajas[1,3,4], Jose Manuel García-Aznar[2], José J Muñoz[5], Pere Roca-Cusachs[1,3]* and Xavier Trepat[1,3,6,7]*

Affiliations:

[1] *Institute for Bioengineering of Catalonia, Barcelona 08028, Spain*
[2]*Aragon Institute of Engineering Research (I3A), University of Zaragoza, 50018 Zaragoza, Spain*
[3]*University of Barcelona, 08028 Barcelona, Spain*
[4]*Centro de Investigación Biomédica en Red en Enfermedades Respiratorias, 28029 Madrid, Spain*
[5]*Laboratory of Numerical Analysis (LaCàN), Polytechnic University of Catalonia (UPC-BarcelonaTech), 08036 Barcelona, Spain*
[6]*Institució Catalana de Recerca i Estudis Avançats (ICREA), Barcelona, Spain.*
[7]*Centro de Investigación Biomédica en Red en Bioingeniería, Biomateriales y Nanomedicina, 28029 Madrid, Spain*

* Correspondence to: rocacusachs@ub.edu, xtrepat@ibecbarcelona.eu

Abstract: The ability of cells to follow gradients of extracellular matrix stiffness – durotaxis– has been implicated in development, fibrosis and cancer. Durotaxis is established as a single cell phenomenon but whether it can direct the motion of cell collectives is unknown. Here we found that multicellular clusters exhibited durotaxis even if isolated constituent cells did not. This emergent mode of directed collective cell migration applied to a variety of epithelial cell types, and required the action of myosin motors and the integrity of cell-cell junctions. By extending traction microscopy to extracellular matrices of arbitrary stiffness profiles we showed that collective durotaxis originated from supracellular transmission of contractile physical forces. To explain the observed phenomenology, we developed a generalized clutch model in which local stick-slip dynamics of cell-matrix adhesions is integrated to the tissue level through cell-cell junctions. Collective durotaxis is far more efficient than single cell durotaxis; it thus emerges as a robust mechanism to direct cell migration during development, wound healing, and collective cancer cell invasion.

One Sentence Summary: Mechanical cooperation between cells enables an emergent mode of collective movement

Main Text:

The ability of living cells to migrate following environmental gradients underlies a broad range of phenomena in development, homeostasis, and disease (*1*, *2*). The best understood mode of directed cell migration is chemotaxis, the well-established ability of cells to follow gradients of soluble chemical cues (*1*). Some cell types are also able to follow gradients in the stiffness of their extracellular matrix (ECM), a process known as durotaxis (*3–10*). Durotaxis has been implicated in development (*11*), fibrosis (*12*) and cancer (*13*), but its underlying mechanisms remain unclear.

Most of our understanding of directed cell migration has been obtained in single isolated cells. However, fundamental processes during development, wound healing, tissue regeneration, and some forms of cancer cell invasion are driven by directed migration of cell groups (*14–16*). Cell-cell interactions within these groups provide cooperative mechanisms of cell guidance that are altogether inaccessible to single cells (*14–20*). Here we investigated whether cell groups undergo collective durotaxis, and the cooperative nature of underlying mechanisms.

Using stencils of magnetic PDMS, we micropatterned rectangular clusters (500 μm width) of human mammary epithelial cells (MCF-10A) on fibronectin-coated polyacrylamide gel substrates exhibiting uniform stiffness or a stiffness gradient (51 ± 17 kPa/mm, Fig. S1) (*21*). Upon removal of the PDMS stencil, clusters migrating on uniform gels displayed symmetric expansion (Fig. 1A,C,E,G, Fig. S2, Movie S1), whereas clusters migrating on stiffness gradients displayed a robust asymmetry characterized by faster, more persistent expansion towards the stiff edge (Fig. 1B-D-F-H, Fig. S2, Movie S1). This result was also

observed in clusters of Madin-Darby canine kidney epithelial cells and 3D spheroids of human epidermoid carcinoma cells (A431) (Fig. S3).

Asymmetric expansion is not attributable to cell proliferation because it was unaffected by inhibition of cell division and because the number of divisions in the cluster was independent of substrate stiffness (Fig. S4). Importantly, it is also not attributable to additive contribution of single cell durotaxis, because single MCF10A cells did not durotax in isolation (Fig. 2A-C,E, Movie S2). Taken together, these data establish an unanticipated mode of collective durotaxis driven by an emergent property of the cell cluster.

Even if single MCF10A cells did not durotax in isolation, they exhibited faster randomly-oriented velocity on stiffer gels (Fig. 2D) (*13*). In a close-packed system, this feature could explain collective durotaxis because volume exclusion would force cells to move persistently away from the cluster at a higher speed on the stiffer edge. To test the contribution of this mechanism, we perturbed cell-cell junctions independently of close packing by knocking down α-catenin using siRNA. As control cells, isolated cells depleted of α-catenin migrated faster on stiffer regions but did not durotax (Fig. S5A-D). Unlike control clusters, however, close-packed clusters depleted of α-catenin expanded nearly symmetrically (Fig. 2F-I, Fig. S5E-M, Movie S3), thereby indicating that cell-cell adhesions are required for collective cell durotaxis. These findings rule out mechanisms solely based on local stiffness sensing and point to a long-range mechanism involving cell-cell adhesion.

We next studied whether this long-range mechanism involves transmission of physical forces across the cluster. To this end, we implemented a generalized traction force microscopy (TFM) algorithm to map forces exerted by cells on substrates with arbitrary stiffness profiles (Supplementary text 1). Clusters migrating on uniform gels (Fig. 3A,C, Movie S4) and on gradient gels (Fig. 3B,D, Movie S5) exhibited similar traction force maps. Highest tractions were localized at the edges and pointed towards the midline of the cluster, whereas relatively lower tractions in the bulk showed no particular orientation. To average out fluctuations and retain systematic traction patterns we computed *x-t* kymographs of traction component T_x (Fig. 3I-J). Kymographs on uniform and gradient gels revealed two traction layers of similar magnitude and opposite sign at both edges of the clusters, and negligible average tractions in the bulk. Interestingly, soft edges had similar cell-substrate forces than stiff edges but smaller and denser cell-matrix adhesions, consistent with previous findings that force levels are not necessarily linked to a specific adhesion size (Fig. S5) (*22*). Unlike traction forces, substrate displacements on gradient gels were nearly one order of magnitude higher on the soft edge than on the stiff one (Fig. 3E,F,K,L, Movies S4-5).

To compute force transmission within the monolayer, we used Monolayer stress microscopy (MSM) and focused on the normal component of the stress tensor in the direction of expansion σ_{xx} (*23*, *24*), which we hereafter refer to as intercellular tension (Fig. 3G-H, Movies S4-5). Kymographs showed that intercellular tension increased up to a plateau within the first few cells at the monolayer edges and then remained roughly constant in the monolayer bulk (Fig. 3M,N).

Together, our force measurements establish that the monolayer expands by generating contractile traction forces of equal magnitude at both edges, and that these forces are transmitted across the cluster. To explore how this physical scenario might lead to collective durotaxis we developed a model that integrates clutch-like cell-ECM dynamics at focal adhesions (*22*, *25–27*), long-range force transmission through cell-cell junctions, and actin polymerization at monolayer edges (Fig. 4A,B, Supplementary text 2). For a monolayer attached to a substrate of uniform stiffness the model predicts symmetric expansion; actin polymerization exceeds acto-myosin contraction to the same extent on both edges. By contrast, on stiffness gradients the substrate deforms and opposes polymerization more on the soft edge, tilting monolayer expansion towards the stiff one (Fig. 4B).

We next used the model to produce testable predictions. Firstly, the model predicts that durotaxis should decrease when reducing the difference in substrate deformation between the soft and stiff side. We confirmed this by reducing the slope of the stiffness gradient (Fig. 4C,D), seeding clusters on progressively stiffer regions of the gradient gels (Fig. 4C,D), reducing cluster size (Fig. S7), inhibiting myosin contractility with blebbistatin (Fig. 4E-H, Fig. S8), and reducing cell adhesion by decreasing fibronectin coating (Fig. S9). Notably, clusters placed one the softest region of the gradient, where the model predicts highest durotaxis, exhibited directed migration towards the stiff edge as a single unit rather than asymmetric expansion (Fig. S10). Secondly, impairing long-range force transmission should abrogate durotaxis. This prediction was confirmed by knocking down α-catenin (Fig. S11, Movie 6) and by laser-ablating clusters in the direction parallel to the midline (Fig. S12), which drastically reduced both intercellular force transmission and durotaxis.

Thirdly, the clutch mechanism implies that actin retrograde flow should be faster on the soft edge, and that the differences between edges in the speeds of actin flow and monolayer expansion should be of the same order. This was indeed verified (Fig. S5). Finally, the model predicts that in response to an extremely steep gradient, even single cells should generate sufficiently large differences in substrate deformation between their leading and trailing edges to enable durotaxis. As predicted, single MCF10A cells exhibited weak but significant durotaxis in response to a step gradient (433 kPa/mm, Fig. S13). Given the close agreement between model predictions and experiments, we conclude that local stiffness sensing at the cluster edges and long range force transmission through intercellular junctions are sufficient to explain the phenomenology of collective cell durotaxis.

Recent experimental and theoretical research has emphasized that some collective systems are more effective at responding to environmental gradients than their isolated constituents (*19*, *20*, *28*). This emergent phenomenon, often alluded to as "collective intelligence", has been observed in cell clusters during chemotaxis (*19*, *20*), fish schools during phototaxis (*28*), and humans groups during online gaming (*29*). In the context of these phenomena, collective durotaxis is unique in that very same machinery that senses the attractant -the actomyosin cytoskeleton- is responsible for propulsion towards it. As such, collective durotaxis might be the most rudimentary and perhaps most primitive mechanism by which a collective living system responds to a gradient. Rudimentary or not, collective durotaxis is robust, general, and dramatically boosts single cell responses, providing a new mechanism to organize directed cell migration during development, wound healing and collective cancer cell invasion.

References and Notes:

1. R. Majumdar, M. Sixt, C. A. Parent, New paradigms in the establishment and maintenance of gradients during directed cell migration. *Curr. Opin. Cell Biol.* **30**, 33–40 (2014).

2. P. Roca-Cusachs, R. Sunyer, X. Trepat, Mechanical guidance of cell migration: lessons from chemotaxis. *Curr. Opin. Cell Biol.*, doi:10.1016/j.ceb.2013.04.010.

3. C.-M. Lo, H.-B. Wang, M. Dembo, Y. Wang, Cell Movement Is Guided by the Rigidity of the Substrate. *Biophysj*. **79**, 144–152 (2000).

4. B. C. Isenberg, P. A. DiMilla, M. Walker, S. Kim, J. Y. Wong, Vascular Smooth Muscle Cell Durotaxis Depends on Substrate Stiffness Gradient Strength. *Biophysj*. **97**, 1313–1322 (2009).

5. M. Raab *et al.*, Crawling from soft to stiff matrix polarizes the cytoskeleton and phosphoregulates myosin-II heavy chain. *J. Cell Biol.* **199**, 669–683 (2012).

6. S. V. Plotnikov, A. M. Pasapera, B. Sabass, C. M. Waterman, Force Fluctuations within Focal Adhesions Mediate ECM-Rigidity Sensing to Guide Directed Cell Migration. *Cell*. **151**, 1513–1527 (2012).

7. T. Kawano, S. Kidoaki, Elasticity boundary conditions required for cell mechanotaxis on microelastically-patterned gels. *Biomaterials*. **32**, 2725–2733 (2011).

8. J. R. Tse, A. J. Engler, Stiffness Gradients Mimicking In Vivo Tissue Variation Regulate Mesenchymal Stem Cell Fate. *PLoS ONE*. **6**, e15978 (2011).

9. L. G. Vincent, Y. S. Choi, B. Alonso-Latorre, J. C. del Álamo, A. J. Engler, Mesenchymal stem cell durotaxis depends on substrate stiffness gradient strength. *Biotechnol. J.*, 8 (2013).

10. L. Bollmann *et al.*, Microglia mechanics: immune activation alters traction forces and durotaxis. *Front. Cell. Neurosci.* **9** (2015), doi:10.3389/fncel.2015.00363.

11. L. A. Flanagan, Y.-E. Ju, B. Marg, M. Osterfield, P. A. Janmey, Neurite branching on deformable substrates. *Neuroreport*. **13**, 2411–2415 (2002).

12. F. Liu *et al.*, Feedback amplification of fibrosis through matrix stiffening and COX-2 suppression. *J. Cell Biol.* **190**, 693–706 (2010).

13. T. A. Ulrich, E. M. de Juan Pardo, S. Kumar, The Mechanical Rigidity of the Extracellular Matrix Regulates the Structure, Motility, and Proliferation of Glioma Cells. *Cancer Res.* **69**, 4167–4174 (2009).

14. D. Cai *et al.*, Mechanical Feedback through E-Cadherin Promotes Direction Sensing during Collective Cell Migration. *Cell*. **157**, 1146–1159 (2014).

15. E. Donà *et al.*, Directional tissue migration through a self-generated chemokine gradient. *Nature*. **503**, 285–289 (2013).

16. A. Haeger, K. Wolf, M. M. Zegers, P. Friedl, Collective cell migration: guidance principles and hierarchies. *Trends Cell Biol.* **25**, 556–566 (2015).

17. A. Bianco *et al.*, Two distinct modes of guidance signalling during collective migration of border cells. *Nature*. **448**, 362–365 (2007).

18. B. A. Camley, J. Zimmermann, H. Levine, W.-J. Rappel, Emergent Collective Chemotaxis without Single-Cell Gradient Sensing. *Phys. Rev. Lett.* **116**, 098101 (2016).

19. G. Malet-Engra *et al.*, Collective Cell Motility Promotes Chemotactic Prowess and Resistance to Chemorepulsion. *Curr. Biol.* **25**, 242–250 (2015).

20. E. Theveneau *et al.*, Collective Chemotaxis Requires Contact-Dependent Cell Polarity. *Dev. Cell*. **19**, 39–53 (2010).

21. R. Sunyer, A. J. Jin, R. Nossal, D. L. Sackett, Fabrication of Hydrogels with Steep Stiffness Gradients for Studying Cell Mechanical Response. *PLoS ONE*. **7**, e46107 (2012).

22. A. Elosegui-Artola *et al.*, Rigidity sensing and adaptation through regulation of integrin types. *Nat. Mater.* **13**, 631–637 (2014).

23. D. T. Tambe, Collective cell guidance by cooperative intercellular forces. *Nat. Mater.* **10**, 469–475 (2011).

24. E. Bazellières *et al.*, Control of cell–cell forces and collective cell dynamics by the intercellular adhesome. *Nat. Cell Biol.* **17**, 409–420 (2015).

25. C. E. Chan, D. J. Odde, Traction Dynamics of Filopodia on Compliant Substrates. *Science*. **322**, 1687–1691 (2008).

26. A. Elosegui-Artola *et al.*, Mechanical regulation of a molecular clutch defines force transmission and transduction in response to matrix rigidity. *Nat. Cell Biol.* **18**, 540–548 (2016).

27. J. Escribano, M. T. Sánchez, J. M. García-Aznar, A discrete approach for modeling cell–matrix adhesions. *Comput. Part. Mech.* **1**, 117–130 (2014).

28. A. Berdahl, C. J. Torney, C. C. Ioannou, J. J. Faria, I. D. Couzin, Emergent Sensing of Complex Environments by Mobile Animal Groups. *Science*. **339**, 574–576 (2013).

29. P. M. Krafft, R. X. Hawkins, A. S. Pentland, N. D. Goodman, J. B. Tenenbaum, in *Proceedings of the 37th Conference of the Cognitive Science Society* (Cognitive Science Society, 2015).

30. J. Alcaraz *et al.*, Microrheology of Human Lung Epithelial Cells Measured by Atomic Force Microscopy. *Biophysj*. **84**, 2071–2079 (2003).

31. M. Dembo, Y. L. Wang, Stresses at the cell-to-substrate interface during locomotion of fibroblasts. *Biophys. J.* **76**, 2307–2316 (1999).

32. J. J. Muñoz, Non-regularised Inverse Finite Element Analysis for 3D Traction Force Microscopy. *Int. J. Numer. Anal. Model.* (2016).

33. C. Selhuber-Unkel *et al.*, Cell adhesion strength is controlled by intermolecular spacing of adhesion receptors. *Biophys. J.* **98**, 543–51 (2010).

34. T. Kim, W. Hwang, R. D. Kamm, Computational Analysis of a Cross-linked Actin-like Network. *Exp. Mech.* **49**, 91–104 (2007).

35. J. Escribano, M. T. Sánchez, J. M. García-Aznar, Modeling the formation of cell-matrix adhesions on a single 3D matrix fiber. *J. Theor. Biol.* **384**, 84–94 (2015).

36. E. A. Novikova, C. Storm, Contractile Fibers and Catch-Bond Clusters: a Biological Force Sensor? *Biophys. J.* **105**, 1336–1345 (2013).

37. F. Kong, A. J. García, A. P. Mould, M. J. Humphries, C. Zhu, Demonstration of catch bonds between an integrin and its ligand. *J. Cell Biol.* **185**, 1275–1284 (2009).

38. M. L. Gardel *et al.*, Traction stress in focal adhesions correlates biphasically with actin retrograde flow speed. *J. Cell Biol.* **183**, 999–1005 (2008).

39. N. Wang, Mechanical Interactions Among Cytoskeletal Filaments. *Hypertension*. **32**, 162–165 (1998).

40. P. Roca-Cusachs, T. Iskratsch, M. P. Sheetz, Finding the weakest link – exploring integrin-mediated mechanical molecular pathways. *J. Cell Sci.* **125**, 3025–3038 (2012).

41. I. Acerbi *et al.*, Human breast cancer invasion and aggression correlates with ECM stiffening and immune cell infiltration. *Integr. Biol. Quant. Biosci. Nano Macro*. **7**, 1120–1134 (2015).

42. C. Storm, J. J. Pastore, F. C. MacKintosh, T. C. Lubensky, P. A. Janmey, Nonlinear elasticity in biological gels. *Nat. Cell Biol.* **435**, 191–194 (2005).

43. J. H. Wen *et al.*, Interplay of matrix stiffness and protein tethering in stem cell differentiation. *Nat. Mater.* **13**, 979–987 (2014).

Acknowledgments:

The authors acknowledge X. Serra-Picamal, V. Romaric and all members of the XT and PR-C labs for stimulating discussions, Natalia Castro for technical assistance, and G. Charras, G. Scita and E. Sahai for providing cells. This work was supported by the Spanish Ministry of Economy and Competitiveness (BFU2012-38146 to XT, BFU2011-23111 to PR-C, DPI2015-64221-C2-1-R to JMG-A, DPI2013-43727-R to JJM, PI14/00280 to DN, RYC-2014-15559 to VC, FPI BES-2013-063684 to JE, IJCI-2014-19156 to AE-A, IJCI-2014-19843 to AL), the Generalitat de Catalunya (2014-SGR-927), and the European Research Council (StG-CoG-616480 to XT, ERC-2012-StG 306751 to JMG-A), Obra Social "La Caixa", Marie-Curie action (CAFFORCE 328664 to AL), EMBO Long-term fellowship (EMBO ALTF 1235-2012 to AL), a Career Integration Grant within the seventh European Community Framework Programme (PCIG10-GA-2011-303848 to PR-C), and Fundació la Marató de TV3 (project 20133330 to PR-C).

Figure legends:

Fig. 1. Cell clusters display durotaxis. (A) A representative cell cluster expanding on a soft uniform gel of 6.6 kPa. Gray transparent area indicates initial cluster position (t=0h) and phase contrast image shows the cluster at 10h. Gray lines indicate cluster edges at 10h. (B) Example of a cell cluster expanding on a gradient gel. Gel stiffness increases towards the right of the panel. Numbers at the bottom indicate Young's modulus values measured with AFM. (C-D) Individual cell trajectories corresponding to the experiments displayed in panels A and B, respectively. Color coding indicates mean cell speed for every track. (E–F) Distribution of the angle θ between the instantaneous velocity vector and the x-axis (see inset) for the experiments displayed in panels A and B, respectively. (G-H) x-t kymographs of cell speed corresponding to the experiments displayed in panels A and B, respectively. Dashed lines indicate initial cluster position. Kymographs were computed by averaging the speed of individual trajectories in the x direction over the y coordinate for every time point (methods).

Fig. 2. Collective durotaxis is an emergent phenomenon. (A) Phase contrast image of MCF-10A cells seeded at low density on a gradient gel. Gel stiffness increases towards the right of the image. Numbers at the top of the panel indicate Young's modulus values measured with AFM. (B) Trajectories of individual cells located in different regions of the gradient gel. For the two regions of the gel, trajectories are plotted with the same origin. Color coding indicates mean cell speed. Mean tactic index (C) and mean speed (D) of single cells located in different regions of the gradient gel (see methods). Horizontal gray bars indicate the stiffness range of each bin. Error bars are SD of n=9-41 cells. (E) Angular distributions of cell trajectories in different regions of the gradient gels. Example of a control cluster (F) and a cluster depleted of α-Cat (G) expanding on a gradient gel. Gray area indicates initial cluster position (t=0h) and phase contrast image shows the cluster at 10h. (H–I) Angular distributions of cell trajectories for experiments shown in panels F and G, respectively. n=5 control and n=7 siRNA α-Cat treated cell clusters with similar stiffness conditions (control and stiffness offset was 47.2 ± 11.9 (mean ± SD) and 39.5 ± 7.3, respectively).

Fig. 3. Traction force microscopy on gradient gels shows long range intercellular force transmission within the clusters. (A-B) Phase contrast images of clusters migrating on a uniform gel (A) and on a gradient gel (B). (C-D) Maps of the traction component T_x for the clusters depicted in A-B. (E-F) Maps of the substrate displacement component u_x for the clusters depicted in A-B. (G-H) Maps of the intercellular tension component σ_{xx} for the clusters depicted in A-B. (I-J) Kymographs of the traction component T_x corresponding to the conditions indicated in A-B. (K-L) Kymographs of the substrate displacement component u_x corresponding to the conditions indicated in A-B. (M-N) Kymographs of intercellular tension component σ_{xx} corresponding to the conditions indicated in A-B. See Supplementary Fig. S14 for all other components of tractions, intercellular stress tensor, and substrate displacements.

Fig. 4. A generalized clutch model predicts collective durotaxis. (A) The expanding cell monolayer is modeled as a one-dimensional contractile continuum that exerts forces on its underlying deformable substrate through discrete focal adhesions and viscous friction. (B, top) Each focal adhesion is modeled as a clutch. Actomyosin-driven contraction of the monolayer causes substrate deformation and actin retrograde flow according to the binding/unbinding dynamics of focal adhesion proteins under force. Substrate deformation is represented as a deformed discrete spring for simplicity but the model is continuum (see Supplementary text 2). (B, bottom) To maintain force balance across the monolayer after each myosin-driven contraction step, the substrate is pulled by a larger amount on the soft side (d_1) than on the stiff side (d_2), thereby tilting overall expansion towards the stiff side ($d_{CM} = d_1 - d_2$). (C) Model predictions. Durotaxis (quantified by the cluster center of mass translation after 10h) represented as a function of the initial stiffness of the center of the cluster (i.e. stiffness offset). (D) Experimental data. Durotaxis (quantified by the cluster center of mass translation after 10h) represented as a function of the initial stiffness of the center of the cluster (i.e. stiffness offset). For steep (red, 56 kPa/mm) and shallow (blue, 14 kPa/mm) gradients, horizontal bars indicate the mean values of the soft and the stiff edge. For uniform stiffness gels (orange), horizontal bars represent the stiffness SD of the gels in the group. Error bars are SD of n=3-9 clusters. (E) Example of a control cell cluster expanding on a gradient gel. (F) Example of a blebbistatin treated cluster expanding on a gradient gel. (G-H) Angle distribution of cell trajectories for control experiments (G) and blebbistatin (H).

List of Supplementary materials:

- Materials and Methods
- Supplementary Text 1
- Supplementary Text 2
- Figures S1-S5
- Table S1
- Captions for Movies S1 to S7
- Movies S1-S7
- References and notes

•

Supplementary Materials for

Collective cell durotaxis emerges from long-range intercellular force transmission

Raimon Sunyer, Vito-Conte, Jorge Escribano, Alberto Elosegui-Artola, Anna Labernadie, Léo Valon, Daniel Navajas, Jose Manuel García-Aznar, José J Muñoz, Pere Roca-Cusachs and Xavier Trepat

correspondence to: rocacusachs@ub.edu, xtrepat@ibecbarcelona.eu

This PDF file includes:

Other Supplementary Materials for this manuscript includes the following:

Materials and Methods

Cell culture

MCF10A cells were maintained in DMEM-F12 media (Life Technologies) supplemented with 5% horse serum, 100 U ml^{-1} penicillin, 100 μg ml^{-1} streptomycin, 20 ng ml^{-1} EGF, 0.5 mg ml^{-1} hydrocortisone, 100 ng ml^{-1} cholera toxin and 10 μg ml^{-1} insulin. MCF10A cells expressing H2B-GFP as a nuclear marker was a kind gift from G. Charras (London Center for Nanotechnology, UK). MCF10A cells expressing H2B-RFP as a nuclear marker was a kind gift from G. Scita (IFOM-IEO Campus, Italy). MDCK strain II cells were cultured in DMEM media (Life Technologies) supplemented with 10% fetal bovine serum, 100 U ml^{-1} penicillin and 100 μg ml^{-1} streptomycin. A431 cells were grown in DMEM media supplemented with 10% fetal calf serum, 100 U/ml penicillin, 100 ug/ml streptomycin. A431 cells were a kind gift from E. Sahai (Francis Crick Institute, UK).

Fabrication of gradient and uniform polyacrylamide gels

To generate polyacrylamide gels with a stiffness gradient, we adapted the slide–mask photopolymerization technique developed by Sunyer and co-workers (*21*). A 30 μl drop of an acrylamide mix (14% acrylamide, 0.94% bis-acrylamide, 0.75 mg ml^{-1} Irgacure, a 1:25 dilution of a saturated solution of (−)riboflavin, 0.56% acrylic acid, and a 1:160 dilution of 0.5 μm fluorescent beads, pH 8.0) was applied to a silanized (3-(trimethoxysilyl)propyl methacrylate) glass bottom petri dish (P35-0-20, Mattek, USA). The solution was covered with a glass coverslip made hydrophobic by treatment with Repel Silane (General Electric, USA).

Gradients were generated by initially covering the acrylamide mix solution with an opaque mask and then slowly sliding it at a controlled speed while irradiating with a UV bench lamp of 365 nm placed at a distance of 6 cm (UVP, USA). The mask was slid using a LabView-controlled (NI, USA) piston of an automatic syringe pump machine (Harvard Apparatus 22, USA). The clamps holding the glass bottom dish and the mask were designed with the opensouce software openScad and 3D printed with a Felix 3.0 printer (FelixRobotix, NL). To ensure complete polymerization, the mask was first slid at a speed of 500 μm s^{-1} for 4 s (uncovering an area for the initial nucleation in the polymerization reaction), and then at 30 μm s^{-1} for 240 s to produce the steep stiffness gradient gels. Shallow gradient gels were produced by sliding the mask at 60 μm s^{-1} for 185 s. After gel photopolymerization, the hydrophobic glass coverslip was removed and the gel was washed with PBS thoroughly to remove unreacted reagents. Every gel was measured with AFM after completing the experiment.

Uniform stiffness polyacrylamide gels were fabricated with the same acrylamide mix solution used to produce stiffness gradients. Instead of polymerizing the solution with the slide–mask technique, we illuminate it homogeneously for a brief period time (from 1min 15s to 1min 40s, at a distance of 1.5 cm from the lamp). This irradiation time ensured a partial polymerization of the solution with final gel rigidities ranging from 5 kPa to 70 kPa. We observed that small differences in the irradiation time (>5s) produced stiffness

differences of tens of kPa. Therefore, the stiffness of every uniform stiffness gel was measured with AFM after completing the experiment.

Gel Functionalization

To promote cell adhesion, fibronectin was covalently linked to the gradient and the uniform gels by crosslinking carboxyl to amine groups. Briefly, gels were immersed in a solution of EDC (0.2 M, (1-ethyl-3-(3-dimethylaminopropyl)carbodiimide hydrochloride), Calbiochem) and NHS (0.1 M, N-hydroxysuccinimide, Sigma-Aldrich) in a MES buffer (0.1 M in milliQ water, pH 5.0, 2-(N-morpholino)-ethane sulfonic acid, Sigma-Aldrich) for 20 min at room temperature. Subsequently, gels were rinsed with PBS and incubated with 0.1 mg/ml of fibronectin for 1h at 37ºC. Next, we washed the gels 3 times with PBS and we incubated them for 15 min with ethanolamine (0.32% in PBS, Sigma-Aldrich) to quench the crosslinking reaction. After washing 3 more times with PBS, gels were stored at 4ºC before use.

Fabrication of magnetic PDMS stencils

Cells were confined to islands with magnetic PDMS. This technique consists in fabricating magnetically attachable stencils made of a mixture of PDMS and magnetite. A magnet underneath the sample secures the magnetic PDMS stencil on the wet polyacrylamide gel while preserving gel protein coating. Briefly, magnetic PDMS was made by mixing thoroughly base and crosslinker in a 10:1 proportion and then adding 20% (w/w) of magnetite (Fe_3O_4, INOXIA Ltd, UK). The mold to fabricate stencils with the magnetic PDMS was made by exposing UV curable nail polish (Sina, UV gel, China) assembled with a transparency mask and exposed to a well-collimated UV laser (488 nm, CrystalLaser, USA). Once poured into the mold, magnetic PDMS was cured at 65ºC overnight. Magnetic PDMS was stored in 70% ethanol after being released from the mold.

Cell patterning on soft substrates

Magnetic PDMS stencils were air-dried, cleaned with an ozone oven (Novascan Ozone Cleaner, USA) and passivated overnight with a sterile solution of 1% Pluronic and 1% BSA in PBS. Before use, magnetic PDMS was washed three times with PBS and air-dried. Cells were confined to islands by placing the magnetic PDMS on top of a gradient or a uniform gel. To secure the magnetic PDMS stencil, we placed a neodymium magnet (Calamit, Italy) underneath the glass-bottom dish with the help of a magnet holder designed and 3D printed in our lab. 30,000 cells in 20 µl media were added to the hollow region defined by the magnetic PDMS stencil. After 1h, more media was added to prevent evaporation. 20h hours after seeding the cells, 2 ml of medium was added and the magnetic PDMS stencils were carefully removed with sterile tweezers before the beginning of the experiment.

Fluorescent time-lapse imaging of cell migration

Fluorescent time-lapse imaging was performed on an automated inverted microscope (Ti-E, Nikon, Japan) equipped with thermal, CO_2 and humidity control, using MetaMorph (Universal Imaging) software. Time-lapse recording started approximately 1h after removing the magnetic PDMS stencil. The interval between image acquisitions was 10 min and a typical experiment lasted between 10 and 15h. During this time we imaged the cells (phase contrast), the fluorescent beads embedded in the gel, and the fluorescent cell nuclei.

To capture the full width of the expanding cell monolayer, two images were acquired at 10× for every time point, approximately overlapping laterally by 20%. Finally, we trypsinized the gels and we obtained a final image of the relaxed position of the beads (reference image).

Image analysis

Fluorescent time-lapse images were accurately stitched with subpixel resolution using Fiji software plugin Pairwise Stitching. We then use a custom-made Matlab script to align and register all images with respect to the reference image. The leading edges of the expanding monolayer were automatically detected by applying a unimodal threshold to the histogram of the phase contrast images. Gel displacements were computed using custom-made particle image velocimetry software on the fluorescent bead images. The interrogation window was 32 × 32 pixels with a window overlay of 0.5. The pixels of the resultant displacement map had an area of 108.16 μm^2.

Nuclei tracking

Individual fluorescent nuclei movement was tracked by means of Fiji using the TrackMate plugin. Cell trajectories were imported in Matlab using the function developed by the Jean Yves Tinevez and analyzed with custom-made scripts.

Quantification of speed and persistence of cell clusters

Let τ be the total recording time of an experiment and $\Delta t = t_k - t_{k-1}$ the time interval between two consecutive images. Over the time period τ, a cell i within a cluster moves $\boldsymbol{r}_i = \sum_k \Delta \boldsymbol{r}_{i,k} = \sum_k (\Delta x_{i,k}, \Delta y_{i,k})$, being $\Delta x_{i,k}$ and $\Delta y_{i,k}$ the distance travelled between the time t_k and the time t_{k+1}. We define the speed along the x axis at time t_k as $v_{x,i}(t_k) = \Delta x_{i,k}/\Delta t$. We define persistence at time t_k as $p_i = \sum_{k-5}^{k} \Delta x_{i,k} / \sum_{k-5}^{k} |\Delta \boldsymbol{r}_{i,k}|$. After appropriate averaging of $v_{x,i}$ and p_i over the cell population, both variables are represented as kymographs (see section Kymographs below). Note that speed and persistence as reported in kymographs are signed variables.

For comparisons, speed and persistence were computed as unsigned variables (unlike kymographs). The average speed of cell i was computed as $v_i = \sum_k |\Delta r_{i,k}|/\tau$. The persistence of cell i was computed as $p_i = L_{i,e}/L_{i,c}$, where $L_{i,e}$ is the Euclidean distance travelled by the cell and $L_{i,c}$ is the contour length of its trajectory.

To perform statistical comparisons between regions within clusters, cellular speed and persistence at the soft and stiff edge of the cluster (Fig. 1P-Q) were averaged by dividing the area of the cluster at t = 0h into 3 adjacent regions (left, center, right). Tracks originated within the left region were counted as soft edge tracks. Tracks originated within the right region were counted as stiff edge tracks.

Tactic index of isolated cell tracks

Tactic index (TI) of an isolated cell i was calculated using the equation (*4*):

$$TI_i = \frac{\sum_k \Delta x_{i,k}}{L_{i,c}}$$

Kymographs

For each pixel in the monolayer, we computed the distance to the closest leading edge. Next we computed the median values of velocities, persistence, tractions, monolayer stresses, and substrate displacements of all pixels located at a given distance from the leading edge. These median values were then represented on a unidimensional segment whose width was the mean width of the monolayer. This operation was repeated for each experimental time point.

Stiffness gradient profile measured with Atomic Force Microscopy

All gradient and uniform gels used in this study were mapped individually using an Atomic Force Microscope (AFM). Briefly, we used a custom-built AFM attached to an inverted optical microscope (Ti-Eclipse, Nikon) as described previously (*30*). Gels were indented with a V-shaped cantilever (Bruker) with a triangular tip. Given the wide stiffness range of the gels, we used a nominal spring constant of k = 0.03 N m^{-1} to ensure that for all measurements, cantilever deflection was within the linear detection range of the AFM. Cantilever spring constant was calibrated by a thermal fluctuation method. The relationship between the photodiode signal and cantilever deflection was computed from the slope of the force displacement curve obtained at a bare region of the coverslip (without gel sample). For each sample, we acquired 5 force–displacement (F–z) curves (where $F = kd$, d being the deflection and z being the piezotranslator position) by ramping the cantilever forward and backward at a constant speed (5 μm amplitude, 1 Hz and ~1 μm of indentation). Each experimental F–z curve was fitted to the four-sided pyramidal indenter model:

$$F = \frac{E \tan\theta}{2^{1/2}(1-\nu^2)}\delta^2$$

where E is the Young's modulus, ν is the Poisson's ratio, θ is the semi-included angle of the pyramidal indenter, and δ is the indentation depth. The parameter ν is assumed to be 0.5, and the indentation depth is calculated as $\delta = z - z_0 - d$, where z_0 is the tip–gel contact point. E and z_0 were estimated by least-squares fitting of this equation to the F–z curve recorded on each gel point. We measured Young's modulus of the gel every 200 μm along the axis of maximum gel stiffness change.

Perturbation of cell–cell adhesions

Cell-cell adhesions were perturbed using the SMARTpool reagents to knock down α-catenin (CTNNA1) as described in (*24*). siRNA transfection was performed by mixing Lipofectamine RNAiMAX with 100 picomoles of a pool of 3 siRNAs and 200,000 freshly trypsinized MCF10A cells (*24*). Cells were then seeded on 6-well plates. Five days after transfection, cells were trypsinized and seeded on stiffness gradient gels.

Inhibitor reagents

Blebbistatin (Sigma-Aldrich) was used at a concentration of 40 μM.

A431 spheroid assay

Cell aggregates were obtained by seeding 5,000 A431 cells on a Ultra Low Attachment 96-well round-bottomed plate (Corning, NY) in a total volume of 200µl of complete media. After 2 days of culture, 500µm diameter spheroids were seeded on the fibronectin-coated gradient gel overnight at 37ºC. Spheroid position within the cluster was achieved with magnetic PDMS stencils.

Supplementary Text 1

Traction Force Microscopy (TFM) on substrates with non-uniform stiffness

Epithelial cell monolayers analyzed in this study migrate on fibronectin-coated polyacrylamide gel substrates polymerized on top of glass coverslips. As a consequence of the forces exerted by the monolayers, the substrates deform elastically. The goal of TFM is to recover cell-substrate tractions from the measured substrate displacements (*31*). Several methods have been described to achieve this goal but they have thus far been applied to substrates of uniform stiffness or with sinusoidal perturbations on the substrate stiffness (*9*). Here we generalize TFM to substrates of arbitrary stiffness profiles.

To that end, domain $D=\{\boldsymbol{x}=(x, y, z) \mid 0 \le x \le L_x,\ 0 \le y \le L_y,\ 0 \le z \le H\}$ denotes the hexahedral substrate region either occupied by the entire gel or analyzed by the microscope. Adherence of the gel substrate to the glass coverslip mathematically translates in a boundary condition on the displacement $\boldsymbol{u}(\boldsymbol{x})$ at the bottom $\Gamma_{bottom}=\{(x, y, z)\in D \mid z=0\}$ as $\boldsymbol{u}(\boldsymbol{x})|_{\Gamma bottom} = \boldsymbol{0}$. Cell monolayer exerts a traction field $\boldsymbol{t}$ on the top surface $\Gamma_{top}=\{(x, y, z)\in D \mid z=H\}$. Gel domain D is assumed to satisfy the following boundary value problem:

$$\nabla\cdot\boldsymbol{\sigma}=\boldsymbol{0},\ \forall\ \boldsymbol{x}\in \mathrm{int}(D) \quad \text{(Cauchy equilibrium equation);} \tag{1}$$

$$\begin{aligned} &\boldsymbol{u}=\boldsymbol{0},\ \forall\ \boldsymbol{x}\in\Gamma_{bottom};\\ &\boldsymbol{\sigma n}=\boldsymbol{t},\ \forall\ \boldsymbol{x}\in\Gamma_{top};\\ &\boldsymbol{\sigma n}=\boldsymbol{0},\ \forall\ \boldsymbol{x}\in\Gamma_{lateral}; \end{aligned} \tag{2}$$

where $\boldsymbol{\sigma}$ is the Cauchy stress tensor, $\boldsymbol{n}$ the external normal to D, and $\Gamma_{lateral}=\{(x, y, z) \mid x=0 \cup x=L_x \cup y=0 \cup y=L_y\}$. It is worth noticing that tractions on the lateral boundary $\Gamma_{lateral}$ may not be exactly zero when the actual gel extends beyond D. This happens, for instance, when D corresponds to the imaging field of a microscope focused on a subdomain of the actual gel substrate. In such cases, the approximation error becomes smaller as D increases in size to cover the entire gel substrate.

Constitutive law of the linear elastic gel substrate reads:

$$\boldsymbol{\sigma}=\lambda\mathrm{tr}(\boldsymbol{\varepsilon})\boldsymbol{\delta}+2\mu\boldsymbol{\varepsilon}$$

where $\boldsymbol{\delta}$ is the second order unit tensor, $\boldsymbol{\varepsilon}=0.5(\nabla\boldsymbol{u}+\nabla\boldsymbol{u}^T)$ the strain tensor, and (λ,μ) the Lamé material parameters. These parameters are not necessarily constant.

We discretize the domain D in n_x, n_y, n_z intervals along the x, y, and z directions respectively. The corresponding mesh is made of $n_x\ n_y\ n_z$ identical hexahedra (finite elements), as shown in Fig. S15.

Standard finite element procedures allow us to approximate the solution of the boundary value problem in (1)-(2) as the solution of the system of equations

$$\mathbf{K}_{\text{top}}\mathbf{u}_{\text{top}} + \mathbf{K}_{\text{in}}\mathbf{u}_{\text{in}} = \mathbf{AMt} \tag{3}$$

where: $\mathbf{u}_{\text{top}}$ is the set of nodal displacements at the top boundary Γ_{top}; $\mathbf{u}_{\text{in}}$ is the set of displacements at all nodes of D except those belonging to Γ_{top} and Γ_{bottom}, that is $D\backslash(\Gamma_{top} \cup \Gamma_{bottom})$; and vector $\mathbf{t}$ contains cell tractions at the nodes in Γ_{top}. Matrices $\mathbf{K}_{\text{top}}$ and $\mathbf{K}_{\text{in}}$ are standard stiffness matrices that couple all the degrees of freedom (dof) of the nodes not in Γ_{bottom}, with respectively the dof at Γ_{top} and $D\backslash(\Gamma_{top} \cup \Gamma_{bottom})$. They have dimensions $[dim(\mathbf{u}_{\text{in}})+dim(\mathbf{u}_{\text{top}})]\times dim(\mathbf{u}_{\text{top}})$ and $[dim(\mathbf{u}_{\text{in}})+dim(\mathbf{u}_{\text{top}})]\times dim(\mathbf{u}_{\text{in}})$, respectively. Matrix $\mathbf{A}$ is a permutation matrix with dimension $[dim(\mathbf{u}_{\text{in}})+dim(\mathbf{u}_{\text{top}})]\times dim(\mathbf{t})$, indicating the loaded nodes, and $\mathbf{M}$ is the mass matrix with unit density associated to Γ_{top} and of dimensions $dim(\mathbf{t})\times dim(\mathbf{t})$. Such quantities explicitly read:

$$\mathbf{K}_{ij} = \int_D \left(\lambda \boldsymbol{\nabla} N_i \boldsymbol{\nabla} N_j^T + \mu(\boldsymbol{\nabla} N_i^T \boldsymbol{\nabla} N_j \mathbf{I} + \boldsymbol{\nabla} N_i \boldsymbol{\nabla} N_j^T)\right) dV;$$

$$\mathbf{A}_{ij} = \begin{cases} \mathbf{I}, \text{if node } i = \text{node } j \in \Gamma_{top} \\ \mathbf{0}, \text{ otherwise} \end{cases};$$

$$\mathbf{M}_{ij} = \mathbf{I} \int_{\Gamma_{top}} pr(N_i) pr(N_j) dS.$$

where $\mathbf{I}$ is the identity matrix, N_i ($\boldsymbol{x}$) is the shape function of node i and $pr(N_i)$ is the projection (or trace) of N_i ($\boldsymbol{x}$) on the boundary Γ_{top}.. Vector $\boldsymbol{\nabla} N_i$ is the gradient of shape function N_i with respect to the coordinates (x, y, z).

The Traction Force Microscopy technique we implement here resorts to the solution of the inverse finite element problem to compute the traction field $\mathbf{t}$ from a set of displacements $\mathbf{u}_{\text{top}}$ measured on Γ_{top}. This traction field $\mathbf{t}$ is obtained by searching a vector $\mathbf{t}$ that satisfies the discrete mechanical equilibrium equation (3) in a least-squares sense. This is mathematically equivalent to solving the minimization problem,

$$\min_{\mathbf{t},\mathbf{u}_{\text{in}}} ||\mathbf{K}_{\text{top}}\mathbf{u}_{\text{top}} + \mathbf{K}_{\text{in}}\mathbf{u}_{\text{in}} - \mathbf{AMt}||^2, \tag{4}$$

The traction $\mathbf{t}$ and displacement $\mathbf{u}_{\text{in}}$ that optimally satisfy equation (4) can be computed by solving the system of equations:

$$\mathbf{K}^{\text{T}}\mathbf{K}\begin{Bmatrix}\mathbf{Mt}\\ \mathbf{u}_{\text{in}}\end{Bmatrix} = \mathbf{K}^{\text{T}}\mathbf{K}_{\text{top}}\mathbf{u}_{\text{top}} \tag{5}$$

where $\mathbf{K}=[\mathbf{A}\ -\mathbf{K}_{\text{in}}]$. It is worth noticing that equation (4) does not resort to any regularization term such as $p||\mathbf{t}||^2$, with p a penalty parameter to be determined. This is due to the uniqueness of the solution of equation (5), which is guaranteed whenever dim($\mathbf{t}$)

$\leq \dim(\mathbf{u}_{top})$ – as it is the case in our examples. The system of equations in (5) may be solved through the staggered procedure (*32*):

$$\begin{aligned} \underline{\mathbf{K}}_{in}^{T}\underline{\mathbf{K}}_{\mathbf{in}}\mathbf{u}_{in} &= \underline{\mathbf{K}}_{in}^{T}\mathbf{K}_{top}\mathbf{u}_{top} \\ \mathbf{t} &= \mathbf{M}^{-1}\mathbf{A}^{T}\left(\mathbf{K}_{top}\mathbf{u}_{top} + \mathbf{K}_{in}\mathbf{u}_{in}\right) \end{aligned} \tag{6}$$

where $\underline{\mathbf{K}}_{in} = [\mathbf{I} - \mathbf{A}\mathbf{A}^{T}]\mathbf{K}_{in}$. The advantage of this procedure is that the matrix of the system of equations in (6), Matrix $\underline{\mathbf{K}}_{in}^{\mathbf{T}}\underline{\mathbf{K}}_{\mathbf{in}}$, is well–conditioned as far as the direct finite element equations in (3) are also well-conditioned. These may be not the case if the aspect ratio of the elements or the differences in the material properties is too large. Conditioning did not affect the accuracy of the results in our tests.

Supplementary Text 2

Generalized Clutch Model description

Recent research has successfully explained the dynamics of cell-matrix interactions through the so-called clutch models (*22*, *25*, *27*). These models have been particularly successful at explaining how the protrusive edge of single cells is able to sense substrate stiffness (*22*, *25*, *27*). It was unclear, however, how clutch models can be expanded to single cells or monolayers with a leading and a trailing edge or, more generally, to cell clusters. Here we developed such generalized model. We started with a model considering only local clutch dynamics, which we implemented and detailed in a previous publication (*27*). Then, we built upon that work to implement a general model that includes long-range force transmission, actin polymerization and cell-substrate friction.

The model is composed by the cell monolayer, the ECM, and adaptor proteins that bind them. It considers cell monolayers as 1D truss elements composed of three parts (Fig. S16A). The first part is a central contractile rod where myosin molecular motors apply forces that contract actin filaments. The second part consists of two adhesive zones flanking the contractile part, which bind to the ECM via discrete particles called adhesion complexes (ACs). Those represent the different adaptor proteins (such as talin, vinculin, paxillin, and integrins) that bind actin to the ECM (*33*). Finally, there is a protrusive part at each monolayer edge, where actin monomers polymerize. This approach thus simplifies the system by considering only the spatial direction along the stiffness gradient, and by assuming that force is transmitted fully through cell-cell contacts at the monolayer bulk, and to the ECM only at monolayer edges. These simplifications are in line with experimental design, and with the observation that forces are on average transmitted to the substrate only at monolayer edges (Fig. 3I-J). We next summarize the different elements of the model and we discuss the numerical implementation of the simulations.

Cell monolayer

The central contractile part of the monolayer was modelled as a long truss element with length $L_{contractile}$ and section $A_{contractile}$ on which myosin exerts a constant contractile force F_m, pulling on the adhesive and protrusive parts. The elastic modulus of the contractile part ($E_{contractile}$(t)) is arbitrarily set so that when myosin contracts the truss, the known inverse relationship between force and actin retrograde speed is reproduced. To this end, $E_{contractile}$(t) is set at each time step so that contraction produced by F_m results in the maximum contraction speed ($v_{contraction,max}$) when divided by the duration of each time step of the model:

$$E_{contractile}\,(t) = \frac{F_m \cdot L_{contractile}(t)}{v_{contraction,max} \cdot \Delta t \cdot A_{contractile}} \qquad (7)$$

Then, actual contraction speed at each time step is determined by the force balance between the myosin pulling force F_m and the opposing force exerted by the substrate through the clutches, F_{AC}:

$$v_{contraction}(t) = \frac{(F_m - F_{AC}(t)) \cdot L_{contractile}(t)}{E_{contractile}(t) \cdot A_{cell} \cdot \Delta t} \quad (8)$$

Hence, if there are no ACs connected to the substrate, transmitted force is zero ($F_{AC} = 0$), and retrograde actin flow speed $v_{contraction}$ is maximum and equal to $v_{contraction,max}$. As ACs connect the cell to the ECM, transmitted force increases and opposes contraction, stalling myosin and actin movement when it reaches F_m. The adhesive part is composed of a set of actin monomers, homogeneously separated between them (d_{act}). We arbitrarily assign a very high elastic modulus to this part ($E_{adhesive}$) to avoid deformation, and its initial length depends on the initial number of actin monomers, n_{am}. The polymerization part is located at the cell edge and grows at a fixed velocity (v_{growth}). The adhesive part is the only one where we explicitly model actin monomers. In each time step, those move rearward with speed $v_{contraction}$, and allow dynamic binding and unbinding of one AC at a time. To model retrograde actin flow across the different parts, every time the polymerization part grows by d_{act} one monomer is transferred to the adhesive part, shrinking the polymerization part to its original length. Analogously, when the contractile part shrinks by 2 d_{act} (one monomer at each side), a monomer is removed from the two adhesive parts and transferred to the contractile part, which grows back to its original length.

Therefore, we note that $E_{contractile}$ and $E_{adhesive}$ merely serve to reproduce a contractile, stiff actin filament and are not meant to represent actual values of cell stiffness.

Substrate

The substrate is simulated as a set of truss elements with total length L_{sub}, and a section A_{sub}. Note that A_{sub} does not match the gel section in experiments since displacements observed in experiments occur not through the entire gel substrate depth but only near the surface. The substrate contains a set of ligand points, which serve as anchoring points for the ACs and are separated a fixed distance, d_{lig}. To model the different stiffness gradient conditions, the stiffness of each truss element E_{sub} (between ligands) is different depending on its spatial location.

Adhesion complexes (ACs)

ACs are modeled as non-symmetric bars in which one end binds to the actin monomers and the other one to the ligands. ACs can thus be completely free and moving according to Brownian dynamics, bound only at one edge, or bound at both edges. Force transmission between cell and substrate only occurs in the latter case. Brownian dynamics of free ACs are governed by the Langevin equation (*34*), in which inertial effects can be neglected. If we consider the i-th AC,

$$\frac{d\boldsymbol{r_i}}{dt} = \frac{1}{\xi_i} \boldsymbol{F_i^B} \quad (9)$$

where $\boldsymbol{r}_i$ corresponds to the current position of the AC, ξ_i is the drag coefficient, and $\boldsymbol{F}_i^B$ is a stochastic force. In order to satisfy the fluctuation-dissipation theorem, the stochastic force, $\boldsymbol{F}_i^B$ is chosen from a random distribution verifying the following expectation values:

$$\langle \boldsymbol{F}_i^B(t)\boldsymbol{F}_j^B(t)\rangle = \frac{2k_BT\xi_i\boldsymbol{\delta_{ij}}}{\Delta t}\boldsymbol{\delta} \tag{10}$$

$$\langle \boldsymbol{F}_i^B(t)\rangle = 0,$$

where k_B is the Boltzmann constant, T the absolute temperature, δ_{ij} is the Kronecker delta, $\boldsymbol{\delta}$ the second order unit tensor and Δt the time increment considered in the simulation. We considered for simplicity that the geometry of the AC corresponds to a sphere with drag coefficient $\xi_{AC} = 6\pi\eta r_{AC}$, with r_{AC} being the radius of the sphere and η the viscosity of the medium (*35*).

Binding and unbinding of ACs from actin and the substrate were modelled through binding rates k_{bind} and unbinding rates k_{ub}^{cb}. Binding rates were modelled according to the Bell equation as a function of the distance between them:

$$k_{bind} = k_{bind}^0 \exp(-\lambda_{bind} \cdot d_b), \tag{11}$$

where λ_{bind} is the mechanical compliance for creating the bond, k_{bind}^0 is the zero-distance binding coefficient and d_b is the distance between the adhesion complex and the closest substrate ligand or actin binding site.

Unbinding was modelled as a catch/slip bond law as has been measured in different integrins (*35*, *36*):

$$k_{ub}^{cb} = \exp(\emptyset_c - \emptyset) + \exp(\emptyset - \emptyset_s) \tag{12}$$

with $\emptyset = F_b/F^*$, where $\emptyset_c$, $\emptyset_s$ are the parameters of the catch and slip bond regimes respectively, F^* is used to normalize the force and F_b is the modulus of the current force for the specific adhesion complex (modulus of the local force transmitted from the cell to the substrate).

Model implementation

Computational simulations were implemented numerically using the Finite Element Method (FEM), under the assumption of small deformations and assuming that all mechanical components present a linear elastic behavior. Nevertheless, a dissipative analysis was required due to the consideration of friction between the cell monolayer and the surrounding medium. All equations are implemented in a C++ code developed by the authors. Simulations begin with all ACs unbound and free, and the monolayer expanding symmetrically at both edges because the speed of actin polymerization dominates over contraction.

For each time increment, the following algorithm is computed after initialization:

1. Solve Langevin equation to calculate AC locations.
2. Check binding events: If ACs are close to substrate ligands or actin monomers, evaluate stochastically whether ACs bind to one of them or both.
3. Compute the displacement field in the substrate and the cell body, due to cell contraction and polymerization.
4. Check unbinding events: from the displacement field we calculate AC forces to determine whether they unbind according to their unbinding probability.

The displacements $\boldsymbol{d}$ at cell monolayer and substrate were calculated through the Finite Element method, considering both elastic forces and a friction coefficient between the cell monolayer and the surrounding medium:

$$\boldsymbol{C\dot{d} + Kd = F} \tag{13}$$

where $\boldsymbol{C}$ is the viscous damping matrix only associated to the cell monolayer (adhesive and protrusive parts), $\boldsymbol{K}$ is the global stiffness matrix and $\boldsymbol{F}$ is the external global force vector. All the components of this external global force vector are zero, except the components corresponding to the degrees of freedom where myosin is exerting the force F_m.

The global stiffness matrix $\boldsymbol{K}$ is built from the assembly of the local stiffness matrix at each element i:

$$\boldsymbol{K^i} = \begin{pmatrix} \frac{E^i A^i}{L^i} & -\frac{E^i A^i}{L^i} \\ -\frac{E^i A^i}{L^i} & \frac{E^i A^i}{L^i} \end{pmatrix} \tag{14}$$

where E^i is the modulus of elasticity of the element (belonging either to the cell adhesive part, the substrate or the adhesion complex), and A^i and L^i are its area and length, respectively.

A particular convenient form of the viscous damping matrix associated to the degrees of freedom of the cell monolayer (in the adhesive/protrusive parts) is the Rayleigh damping matrix:

$$\boldsymbol{C^i} = \frac{\varsigma}{\rho}\boldsymbol{M^i} = \frac{1}{2}\,\varsigma L^i \begin{pmatrix} 1 & 0 \\ 0 & 1 \end{pmatrix} \tag{15}$$

where ς is the friction coefficient associated to the surrounding medium[1], ρ is the density of the cell monolayer and $\boldsymbol{M}$ is the diagonal mass matrix associated to the cell monolayer.

To solve the mechanical problem, we use a backward Euler method:

$$\boldsymbol{C}\boldsymbol{v}_{n+1} + \boldsymbol{K}\boldsymbol{d}_{n+1} = \boldsymbol{F}_{n+1} \quad (16)$$

$$\boldsymbol{v}_{n+1} = \frac{\boldsymbol{d}_{n+1} - \boldsymbol{d}_n}{\Delta t} \quad (17)$$

where $\boldsymbol{d}_n$ and $\boldsymbol{F}_{n+1}$ are the approximations of $\boldsymbol{d}(t_n)$ and $\boldsymbol{F}(t_{n+1})$ respectively. In particular, we have implemented the d-form:

$$\frac{1}{\Delta t}(\boldsymbol{C} + \Delta t\, \boldsymbol{K})\boldsymbol{d}_{n+1} = \boldsymbol{F}_{n+1} + \frac{1}{\Delta t}\boldsymbol{C}\boldsymbol{d}_n \quad (18)$$

Modelling results and different experimental conditions

Once the model was implemented, it systematically led to monolayers expanding with time faster on the stiff than on the sot edge, leading to a progressive displacement of the center of mass to the stiff side of the gradient (Fig. S16B). To simulate the different experimental conditions, we use the model parameters indicated in Tables S1 and S2. The only parameter tuned for the different conditions is the elasticity modulus of the substrate, in order to reproduce the corresponding stiffness gradient and the initial monolayer stiffness offset. Additionally, simulations with different ligand densities and monolayer widths were also carried out to model experiments analyzing the effect of fibronectin coating and pattern width, respectively.

To model the effect of α-catenin depletion, monolayers were not modelled as a single element containing one contractile region flanked by two adhesive and protrusive zones, but as several of those elements (representing individual cells) linked together. To prevent cells from stepping on each other, cell-cell interactions were simulated by means of springs joining the edges of actin filaments of two cells. In those conditions, cell-ECM adhesions and force transmission were now enabled across the monolayer and not only at the edges (Fig. S16C). Paralleling experiments, introducing seven or more elements instead of only one led to cell-ECM force transmission across the entire monolayer, and not only at the edges (Fig. S16D-E). The resulting loss of long range intercellular force transmission drastically reduced durotaxis in response to the same rigidity gradient (Fig. S16F).

Table S1 Physical model parameters

Parameter	Symbol	Value
Boltzman energy	$k_B T$	$4{,}142 \cdot 10^{-21}$ (J)

[1] This friction coefficient is fixed to be kg/nm.s to assure adequate units of $\mathbf{C}^i$ as kg/s.

		(*34*)
Myosin force	F_m	800 (pN) (*22*, *26*)
Unloaded contraction velocity	$v_{contraction}$	80 (nm/s) (*22*, *26*)
AC stiffness	$K_{AC} = \frac{E_{AC}A_{AC}}{L_{AC}}$	15 pN/nm
Force to normalize parameters in catch bond law	F^*	3 (pN) (*37*)
Nondimensionalized force of catch curve in catch bond law	$\emptyset_c$	0.6025 (*37*)
Nondimensionalized force of slip curve in catch bond law	$\emptyset_s$	10.2112 (*37*)
Actin polymerization velocity	v_{growth}	12 (nm/s) (*38*)
Mechanical compliance of the AC for creating the bond	λ_{bind}	0.1 (nN^{-1}) (*22*)
Zero-force binding coefficient	k_{bind}^0	100 (s^{-1}) (*22*)
Medium viscosity for cell-susbtrate dispalcements	ς	$1.16 \cdot 10^3$ (Pa.s) (*39*)
Medium viscosity for the AC arm	η	$8.599 \cdot 10^{-4}$(Pa·s) (*34*)

Model parameters are within the range of values previously measured and used in former models in the literature (see references in table). Myosin forces and myosin contraction speeds are of the order of our previous measurements (speeds) and model parameters (forces) (*22*, *26*). The stiffness of the AC is of the order of reported values for integrin-actin linkers (*40*). The binding coefficients used (λ_{bind}, k_{bind}^0) are also of the order of previously measured fibronectin-integrin binding rates when evaluated at the typical distances enabling binding (10^1-10^2 nm) (*22*). Catch bond parameters are of the order of previously reported values for α5β1 (*37*). Actin polymerization velocities are of the order of measured actin flows upon myosin inhibition, which are driven by actin polymerization (*38*). The medium viscosity for cell-substrate displacements is of the order of estimated cytoskeletal viscosities (*39*). To model AC diffusion, we employed typical viscosities of aqueous media as previously done (*34*).

Table S2 Technical model parameters

Simulation Parameter	Symbol	Value
Cell contractile part elastic modulus	$E_{contractile}$	$3.05 \cdot 10^6$(Pa)
Cell adhesive part elastic modulus	$E_{adhesive}$	$5 \cdot 10^7$ (Pa)
Cell adhesive part length	$L_{adhesive}$	$6 \cdot 10^3$ (nm)
Monolayer length	$L_{monolayer}$	$5 \cdot 10^5$ (nm)
Cell area	A_{cell}	$8 \cdot 10^5$ (nm^2)
Distance between actin monomers	d_{am}	25 (nm)
Substrate length	L_{sub}	$2.5 \cdot 10^6$ (nm)

Substrate area	A_{sub}	$2.2 \cdot 10^7$ (nm^2)
Distance between ligands	d_{lig}	100 nm
Simulation step time	Δt	0.03 s
Total time of the simulation	$\boldsymbol{T}$	**360 s**

Parameters above were chosen simply to reflect the length and time scales involved in experimental conditions. We note that $E_{contractile}$ and $E_{adhesive}$ do not reflect actual cell parameters but serve merely to model a rigid actin filament ($E_{adhesive}$) and to reproduce the experimental inverse force/speed relationship of actin flow (see cell monolayer section above).

Model limitations and critique

This model was built to test the hypothesis that durotaxis can be driven by the observed long-range force balance, simply by generating different deformations on soft versus stiff regions of the substrate. Model results confirm this hypothesis, which we further verified experimentally by regulating monolayer width, myosin activity, or fibronectin coating to perturb differential substrate deformation. The model was implemented in a reduced, simplified one-dimensional setting precisely to test the generality of our hypothesis. However, we note that this simplicity precludes the model from predicting some of the observed behavior. Due to its one-dimensional nature the model does not consider individual cells, or their spatial distribution of adhesion complexes. Thus, the model does not predict how substrate stiffness regulates cell density, or the formation, maturation, and distribution of cell-matrix adhesions within cells. Those parameters were indeed affected by stiffness, since stiffer regions had reduced cell density (Fig. X) and larger cell-matrix adhesions (Fig. X), which is consistent with previous work (REF Elosegui Artola 2014, 2016). Whereas it is clear that those parameters may influence cell migration, we note that in terms of durotaxis they act upstream of force transmission, determining whether it can be established or not. Once established (as we measured), durotaxis emerges naturally irrespective of the specific means of cell-substrate force transmission. Further, we note that both cell spreading and size are local properties also regulated by stiffness in single cells, which nevertheless do not durotax except in extremely steep gradients.

Supplementary Text 3

Supplementary discussion

The stiffness of living tissues varies several orders of magnitude across the animal body (*3–13*). Brain, bone marrow, and embryonic tissues are the softest tissues reported thus far (0.2-0.6 kPa) while bone and cartilage are the stiffest ones (25-100 kPa). Within this broad spectrum, liver, kidney, fat and lung are considered relatively soft (1-6 kPa), while heart and muscle are relatively stiff (12-20 kPa). Tissue stiffness is severely affected in diseases associated with synthesis and remodeling of the ECM. For example, the stiffness of the lung parenchyma of normal mice was reported to be ~0.5 kPa, whereas that of fibrotic tissue of bleomycin-treated lungs was ~3 kPa with peaks >15kPa (*12*). The stiffness of infarct scar was found to be 30-70 kPa, markedly stiffer than heart muscle (*5*, *9*). In cancer, tumors have been extensively shown to be stiffer than their surrounding tissue (generally 1-10 kPa) and stiffness is highest at invasive fronts (*41*).

The broad heterogeneity of stiffness within and between tissues naturally leads to stiffness gradients (*3–13*). While a systematic characterization of these gradients is still lacking, Engler and co-workers proposed that they could be generally classified as physiological (1 kPa/mm), pathological (10 kPa-40/mm kPa/mm), and interfaces (>100 kPa/mm) (*9*). Here we analyzed collective epithelial durotaxis in the presence of shallow gradients (14 kPa/mm) and steep gradients (51 kPa/mm). According to the data discussed above, gradients of this order of magnitude are relevant in processes involving collective cell migration such as reepithelialization in wound healing and collective cancer invasion.

Even if the gradients analyzed in our study were relatively steep, they were insufficient to enable durotaxis of epithelial cells in isolation. Only in the presence of extremely steep gradients (433 kPa/mm), MCF10A cells exhibited single cell durotaxis with a directed velocity of 0.066 μm/min (x component of the Euclidean velocity). This value is smaller than that obtained for single MSCs on similar gradients (~0.3 μm/min, 275 kPa/mm) and single microglial cells on much shallower gradients (~1 μm/min, 8 kPa/mm). Importantly, the velocity of single MCF10A cells on extreme gradients is also smaller than the velocity at which the center of mass of MCF10A clusters advances on shallow (~0.071 μm/min, 14.3 kPa/mm) and steep gradients (~0.14 μm/min, 51 kPa/mm). Thus MCF10A cells undergo collective durotaxis faster than single cells on much steeper gradients, and they do so with a speed of the same order of magnitude than single MSCs.

All our experiments were conducted on polyacrylamide gels coated with fibronectin. These hydrogels gels have been shown to exhibit a linear stress/strain relationship up to ~100% strain (*42*). By contrast, most physiological ECM gels are highly non-linear (*42*). This is the case, for example, of collagen and fibrin, which show pronounced strain-stiffening above 10-20% strain. Given that durotaxis is ultimately driven by differences in matrix displacements, strain-stiffening will surely affect durotaxis efficiency in physiological ECMs. This effect should be particularly critical on soft ECMs, where displacements and strains will be larger, and cell forces will push hydrogels towards their non-linear regime. Our study raises the question as of whether physiological non-linearities will discourage

durotaxis (by increasing the stiffness offset) or favor it (by increasing gradient steepness). We also note that, in general, biological processes can be influenced by the porosity of the ECM. However, the close agreement between model predictions and experimental data supports that durotaxis originates from a stiffness gradient rather from a porosity gradient (*43*).

Supplementary Figure S1

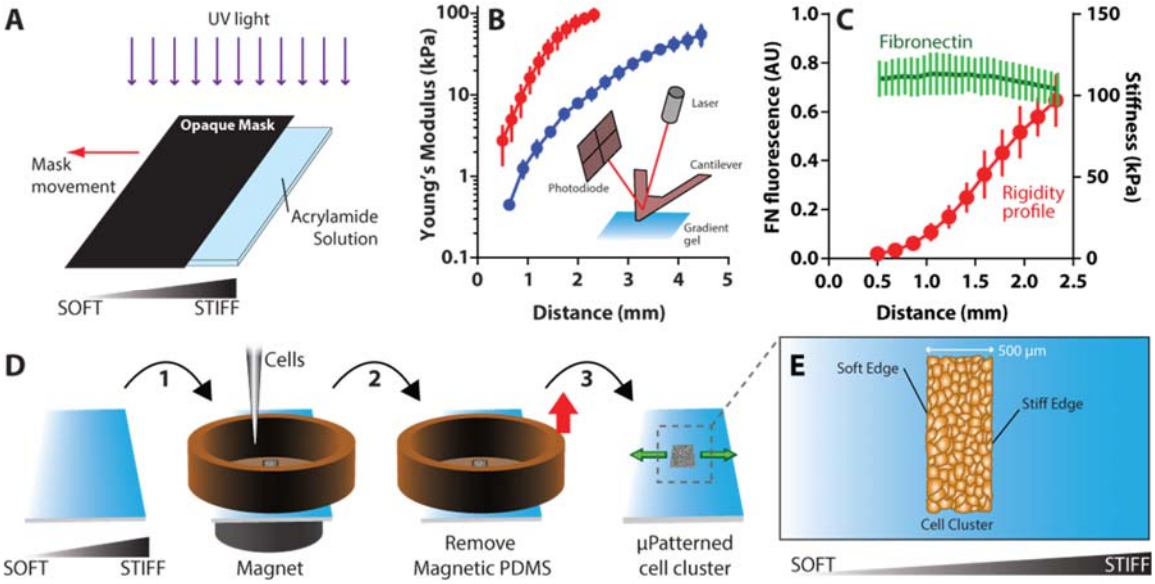

Figure S1. (A) To produce stiffness gradient gels, we irradiate an acrylamide/bis-acrylamide solution containing irgacure. Initially, the sample is protected by an opaque mask. An irradiation gradient is obtained by moving the mask (in the direction of the arrow) while illuminating the solution with a non-collimated UV lamp (365 nm). (B) Gel stiffness profile measured with AFM. The origin of the distance indicates the softer edge of the gel. Error bars represent SD of n = 5-10 gels. (C) Average fluorescence intensity profile of fibronectin along gradient gels (green). Spatial variation of gel elasticity (red). Error bars represent SD of n = 6 gels. (D) To micropattern a cell cluster, a magnetic PDMS stencil with a rectangular opening is placed on top of a polyacrylamide gel (step 1). A magnet below the bottom coverslip is used to attract the magnetic PDMS and seal the stencil on the wet polyacrylamide gel. After overnight incubation, the magnetic PDMS is released (step 2) and the expansion of the resulting micropatterned cluster is monitored by time lapse microscopy (step 3). (E) Scheme of the experiment at the onset of cell migration.

Supplementary Figure S2

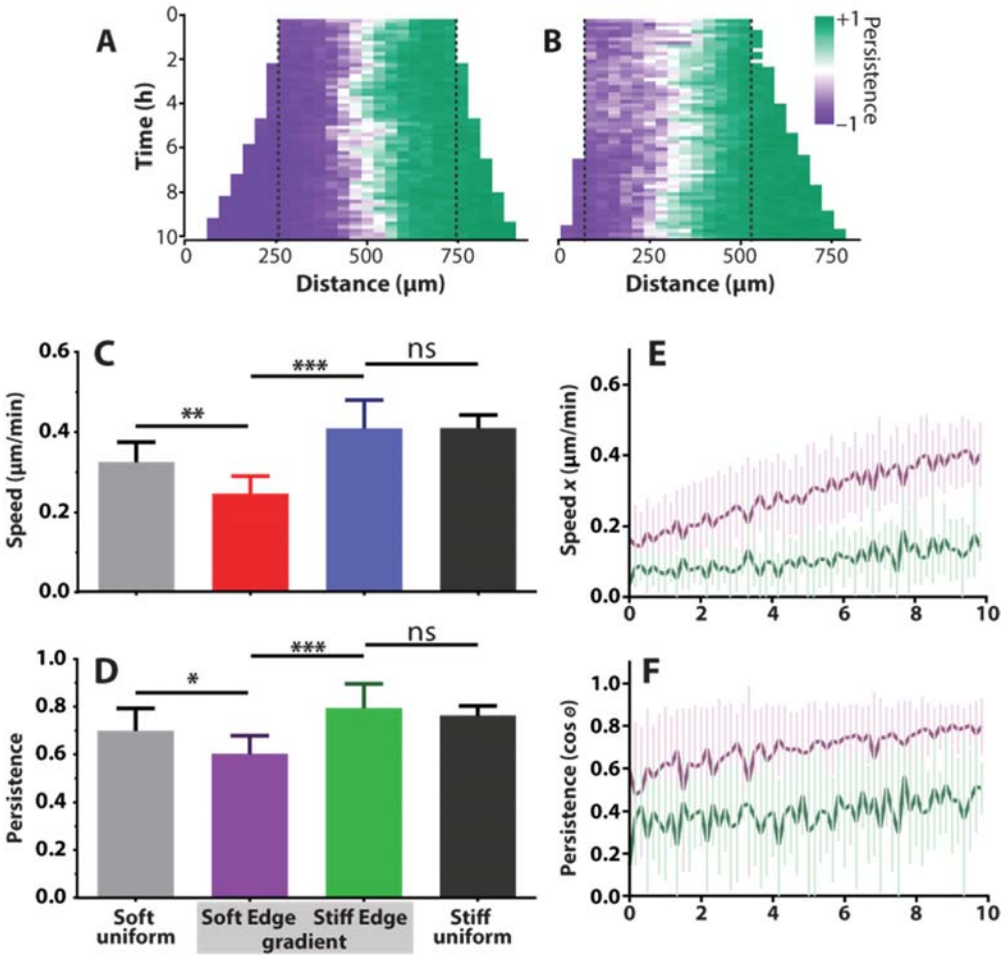

Figure S2. (A-B) Kymographs of cell persistence corresponding to the experiment displayed in Fig. 1A and Fig. 1B, respectively. Dashed lines indicate initial cluster position. Cellular speed (C) and persistence (D) at the soft and stiff edges averaged over experiment repeats (see methods). For comparison, persistence is plotted unsigned. (E-F) Speed and persistence of cells at the soft and stiff edges as a function of time. In C-F error bars are SD of n=6 soft uniform gels (9.4 ± 4.1 kPa, mean ± SD), n=6 stiff uniform gels (34 ± 20.9 kPa) and n=9 stiffness gradient gels (stiffness offset 25.9 ± 6 kPa).

Supplementary Figure S3

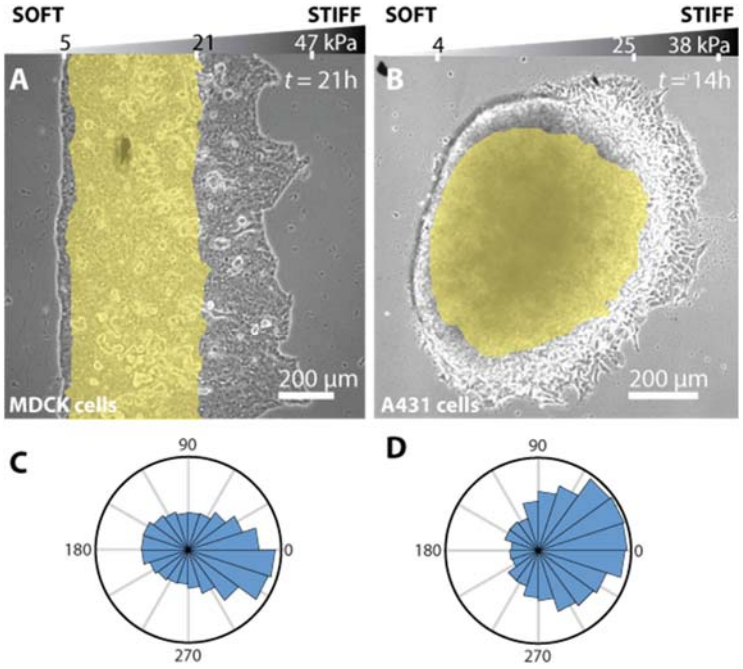

Figure S3. Collective durotaxis in clusters of MDCK cells and spheroids of A431 cells. A cluster of MDCK cells (A) and a spheroid of A431 cells (B) migrating on a gradient gel. Gel stiffness increases towards the right of the panel. Yellow areas indicate the initial cluster/spheroid position (t=0h) and phase contrast images show the clusters at 21h and 14h, respectively. (C-D) Angle distribution at every time step (10 min) for MDCK clusters and A431 spheroids, respectively.

Supplementary Figure S4

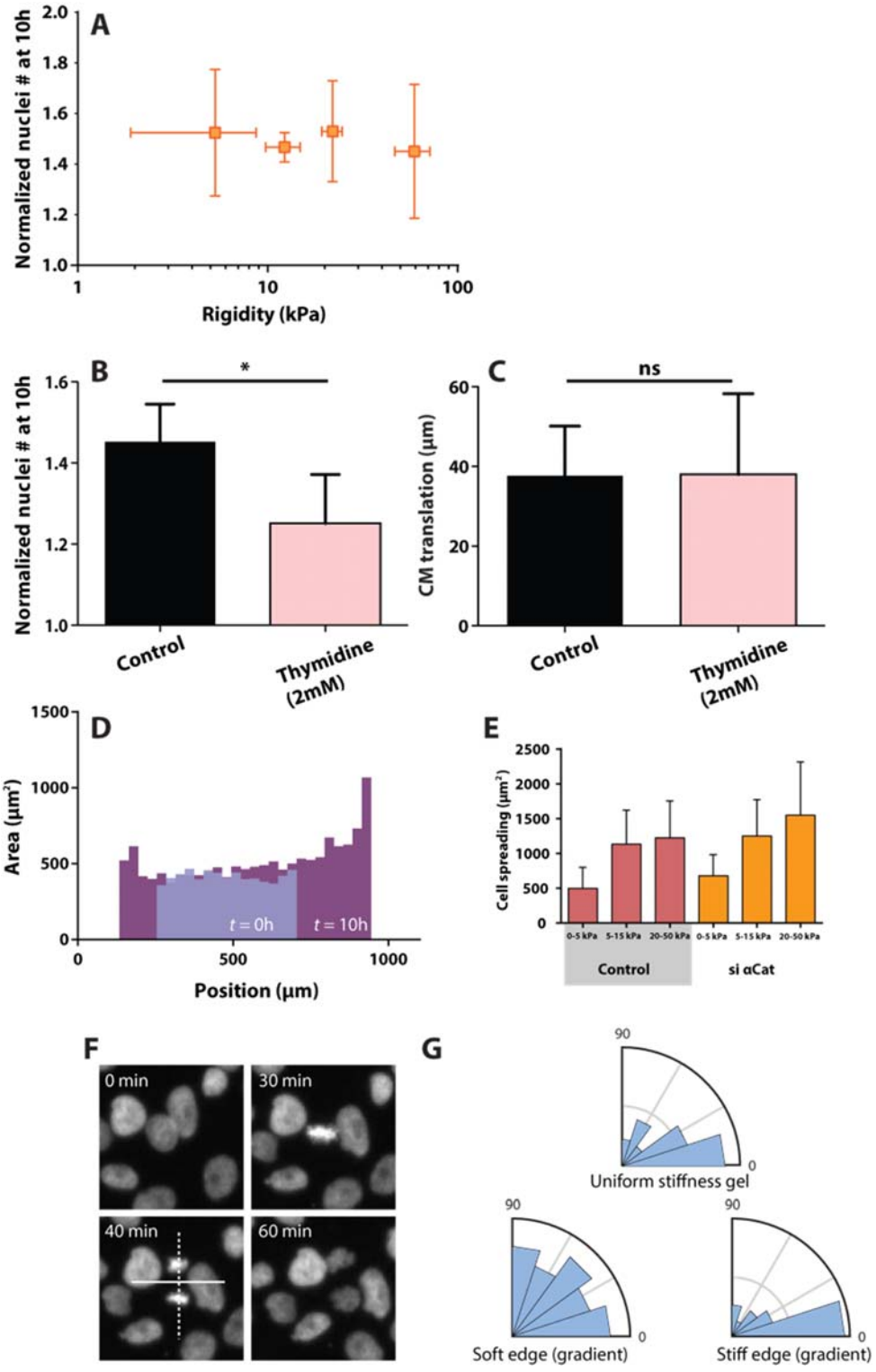

Figure S4. (A) Cell proliferation in clusters after 10h for different rigidity conditions (mean ± SD of n=3-9 clusters). (B) Number of cells after 10h of expansion in control clusters and in clusters in which cell division was inhibited with thymidine. (C) Translation of the center of mass of control clusters and of clusters in which cell division was inhibited with thymidine. These data show that collective durotaxis is not attributable to cell division. (D) Average cell area as a function of the *x* position in the cluster at the onset of experiments and after 10h of expansion. These experiments show that initial cell density was insensitive to local substrate stiffness. With time, faster cells increased their area as a direct consequence of continuity of the monolayer. (E) Spreading area of isolated control cells and isolated cells depleted of α-catenin. In both cases, cells showed higher spreading on stiff gels than on soft ones, yet only control cells exhibited collective durotaxis. These results indicate that local adaptation of cell area to substrate stiffness does not mediate collective durotaxis. (F) Cell division was more oriented with the x-axis on the stiff area of the cluster than on the soft one. Inhibition of cell division did not affect durotaxis, however (see C), thus showing that differences in oriented cell division are not the cause of collective durotaxis.

Supplementary Figure S5

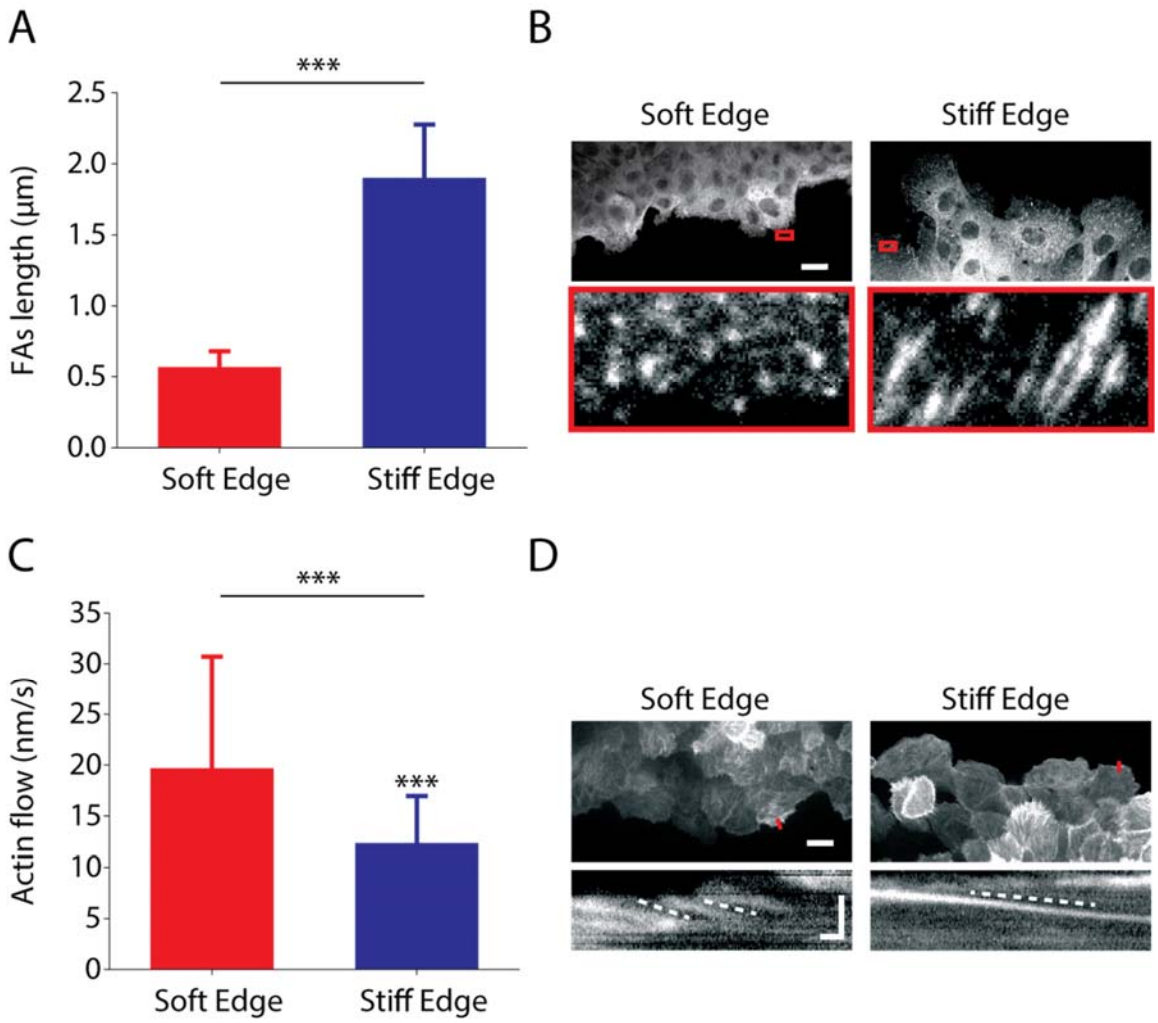

Figure S5. (A) Quantification of focal adhesion length (paxilin) measured on the soft and stiff edges of gradient gels (n=22 and 21 cells on the soft and stiff edge, respectively, measured on 2 different gradient gels). Significant differences were observed between the soft and the stiff edge (*** P<0.001, student's t-test). (B) Representative paxilin images on the soft and stiff edge of a gradient gel. Scale bar is 20 μm in the main images and insets are 10.6 × 5.3 μm. (C) Quantification of actin rearward flow speeds for cells on the soft and the stiff edge of gradient gels (n=43 and 40 cells on the soft and stiff edge, respectively, measured on 4 different gradient gels). Significant differences were observed between the soft and the stiff edge (*** P<0.001, student's t-test). (D) Representative MCF10-A LifeAct-GFP images on the soft and the stiff edge of a gradient gel. Insets are kymographs showing the movement of actin along the discontinuous lines marked in withe. Scale bar is 20 μm in the main images and 10 s / 3 μm (x/y axes) in the kymographs. Error bars, SD.

Supplementary Figure S6

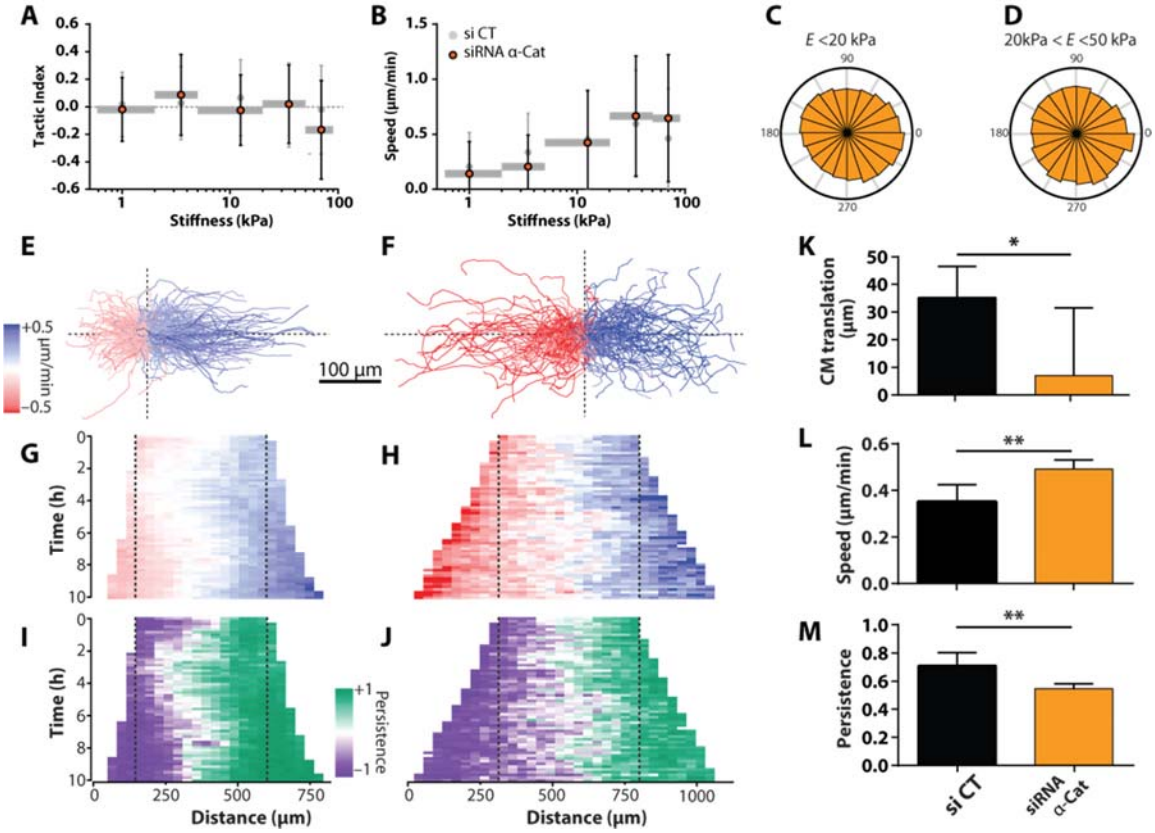

Figure S6. Inhibition of cell-cell junctions impairs collective durotaxis. (A-B) Mean tactic index (A) and mean speed (B) in different regions of the gradient gel for siRNA control and αCat depleted single cells. Error bars are SD of n=6-25 cells. (C-D) Angular distributions of the trajectories of α-Cat depleted cells in different regions of the gradient gels. (E–F) 10h individual cell tracks for the experiments shown in Fig. 2F and 2G, respectively. All tracks are plotted with a common origin. Color coding indicates the mean track speed. Speed (G–H) and persistence (I–J) kymographs for experiments shown in Fig. 2F and 2G, respectively. Color coding of speed kymographs is the same as in panel E. (K) Durotaxis (quantified by the cluster center of mass translation after 10h) of control and α-Cat depleted clusters. Mean cluster speed (L) and mean cluster persistence (M) averaged over experimental repeats for control siRNA cell clusters and cell clusters depleted of α-Cat (see methods). For comparison, persistence is plotted unsigned. For panels K–M, error bars are SD of n=5 control and n=7 siRNA α-Cat treated cell clusters with similar stiffness conditions (control and stiffness offset was 47.2 ± 11.9 (mean ± SD) and 39.5 ± 7.3, respectively).

Supplementary Figure S7

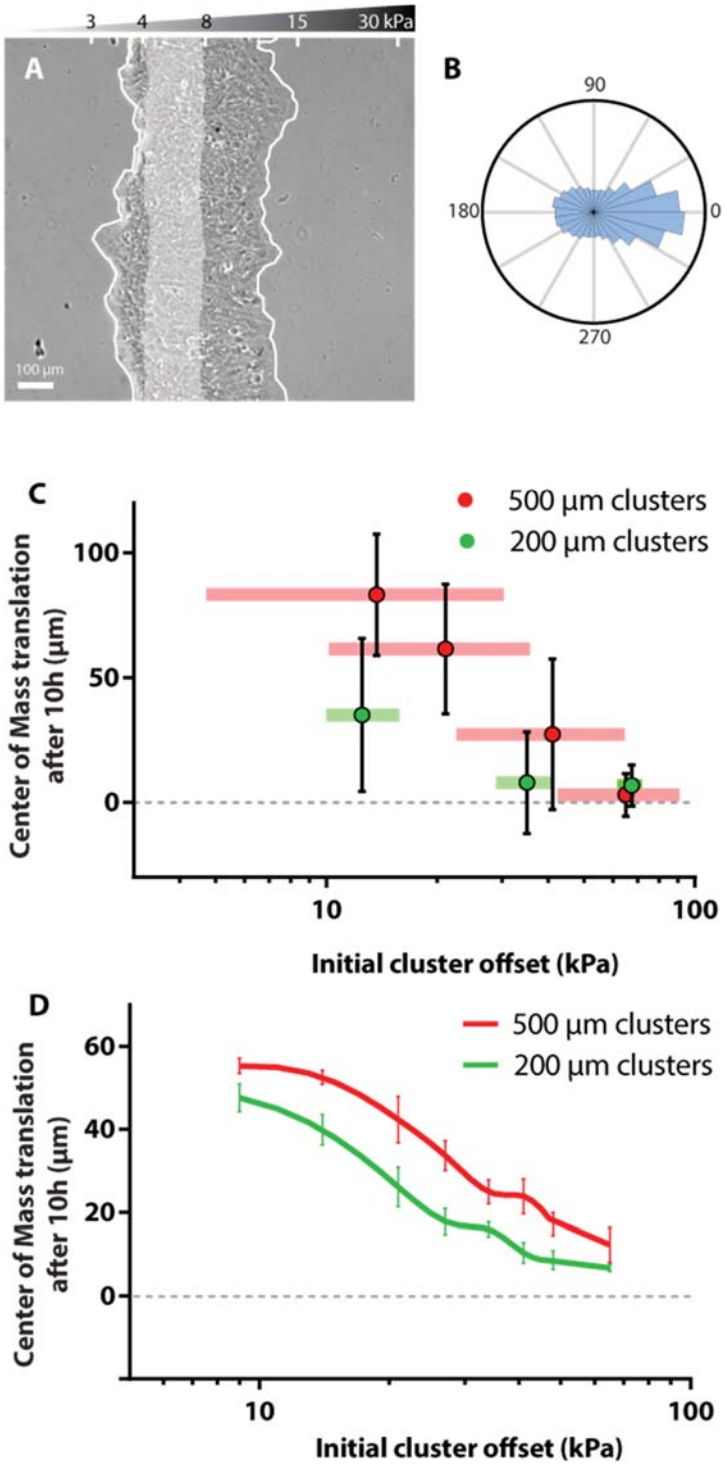

Figure S7. Collective durotaxis increases with cluster size. (A) A 200 μm representative cell cluster expanding on a gradient gel. Gray transparent area indicates initial cluster position (t=0h) and phase contrast image shows the cluster at 10h. Gray lines indicate cluster edges at 10h. (C) Durotaxis (quantified by the cluster center of mass translation after 10h) represented as a function of the initial stiffness of the center of the cluster (i.e. stiffness offset) for 500 μm (red) and 200 μm (green) clusters. Horizontal bars indicate the mean values of the soft and the stiff edge. n=3-4 clusters. (D) The model captures the results shown in (C).

Supplementary Figure S8

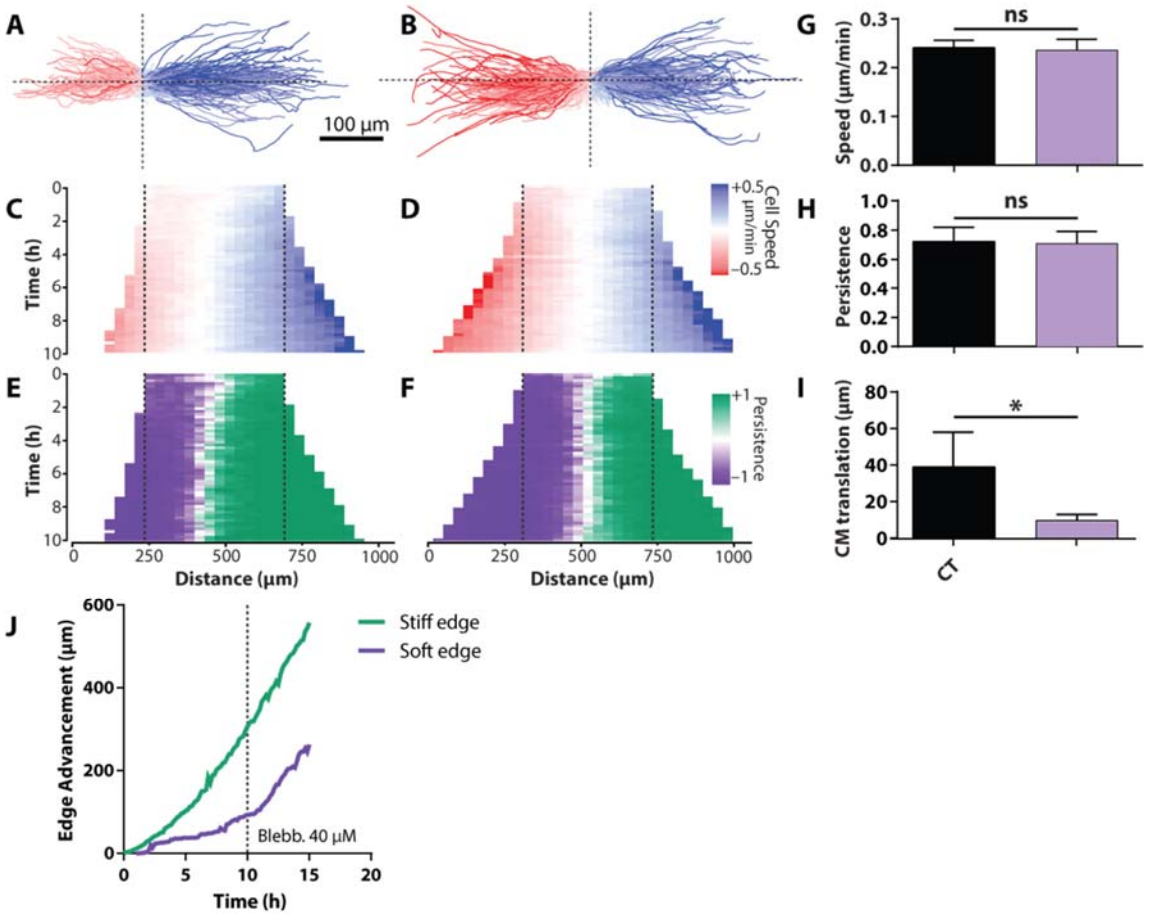

Figure S8. Inhibition of cell contractility impairs collective durotaxis. (A–B) 10h individual cell tracks for experiments shown in Fig. 4E and Fig. 4F, respectively. For clarity, tracks are plotted with a common origin. Speed (C–D) and persistence (E–F) kymographs for experiments shown in Fig. 4E and 4F, respectively. Mean speed (G) and mean persistence (H) obtained after averaging over experimental repeats for control and blebbistatin treated clusters. (I) Durotaxis (quantified as cluster center of mass translation after 10h) of control and blebbistatin treated clusters. For panels G-I, error bars are SD of n=4 control and n=3 blebbistain treated cell clusters with similar stiffness conditions (control and stiffness offset was 26.4 ± 5.5 (mean ± SD) and 25.7 ± 6.7, respectively).

Supplementary Figure S9

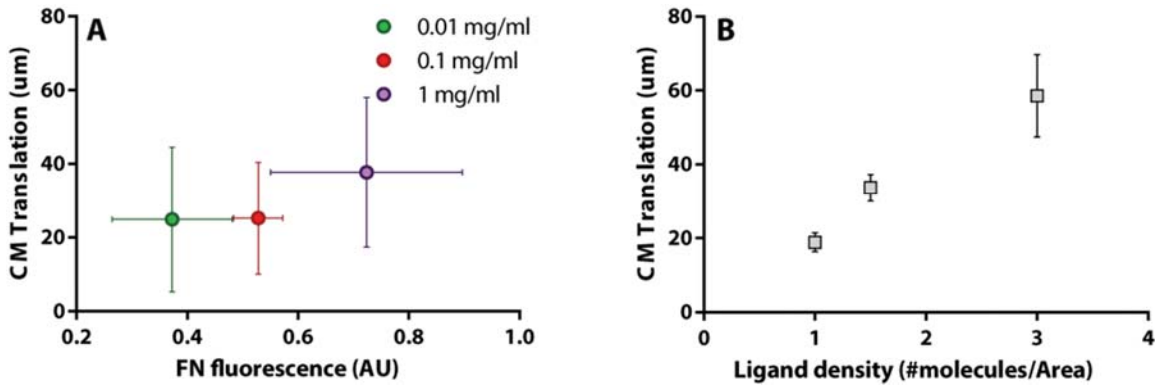

Figure S9. Collective durotaxis tends to increase with ECM density. (A) Durotaxis (quantified as cluster center of mass translation after 10h) of 500 μm clusters expanding on gels coated with three different densities of fibronectin. For each experiment, fibronectin density was measured using immunofluoresence. (B) The model predicts an increase in collective durotaxis with increasing ligand density.

Supplementary Figure S10

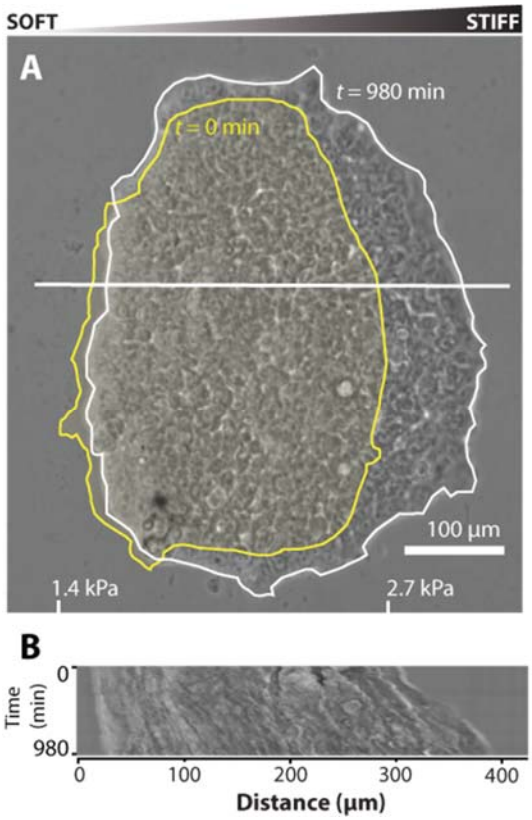

Figure S10. Clusters seeded on gradients with low stiffness offset displayed directed migration as a single unit rather than asymmetric expansion. (A) A representative cluster at t=0 min (yellow contour) and t=980 min (white contour and phase contrast image) seeded on the softest region of a gradient gel. (B) Kymograph of phase contrast images. See also Movie SXXX.

Supplementary Figure S11

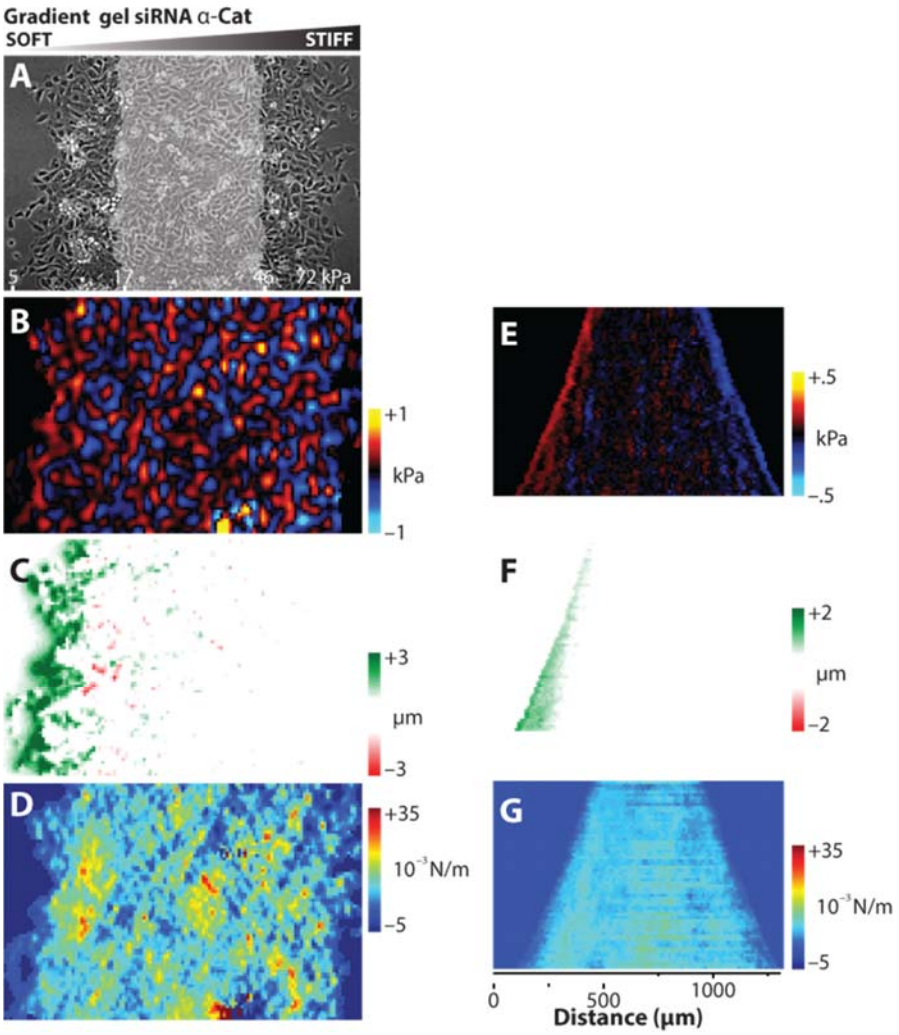

Figure S11. Mechanics of α-cat depleted clusters migrating on a gradient gel. (A) Phase contrast image. (B) Map of the traction component T_x for the cluster depicted in A. (C) Map of the substrate displacement component u_x for the cluster depicted in A. (D) Map of the intercellular tension component σ_{xx} for the cluster depicted in A. (E) Kymograph of the traction component T_x corresponding to the conditions indicated in A. (F) Kymograph of the substrate displacement component u_x corresponding to the conditions indicated in A. (G) Kymograph of intercellular tension component σ_{xx} corresponding to the conditions indicated in A-C. See Supplementary Fig. S14 for all other components of tractions, intercellular stress tensor, and substrate displacements.

Supplementary Figure S12

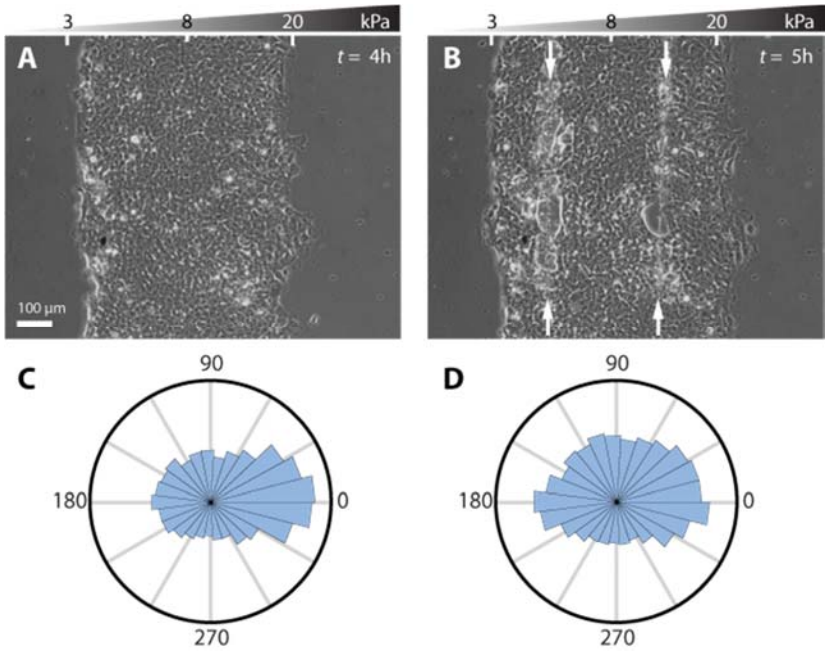

Figure S12. Longitudinal severing of the monolayer impairs collective durotaxis. (A-B) An expanding cluster before (A) and one hour after ablating the monolayer with two laser cuts parallel to the monolayer midline (B, white arrows, see Movie XXXXX). (C-D) Angular distributions of cell trajectories before (C) and after (D) ablation (see methods). These results further support that long range force transmission enables collective durotaxis.

Supplementary Figure S13

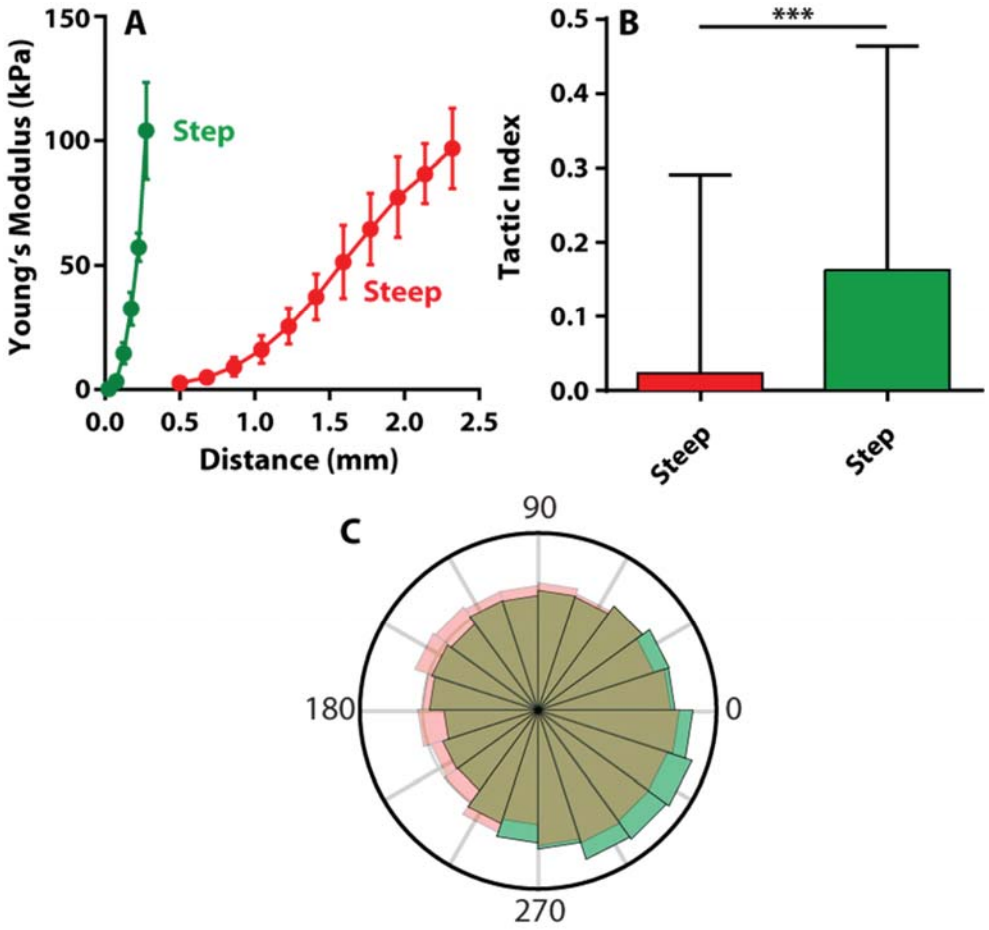

Figure S13. Single isolated MCF10A cells show weak but significant durotaxis on extreme stiffness gradients. (A) AFM characterization of steep (56 kPa/mm) and step (433 kPa/mm) gradients. (B) Contrary to the case of cells migrating in isolation on steep gradients, cells migrating on step gels showed weak but significant durotaxis. (C) Angular distribution of single cell trajectories on steep and step gradients. Note that the net velocity produced by single cell durotaxis on step gradients is lower than that produced by collective durotaxis on steep and shallow gradients (see Supplementary discussion). Single cell durotaxis on extreme gradients is well captured by the clutch model described in Supplementary text 2.

Supplementary Figure S14

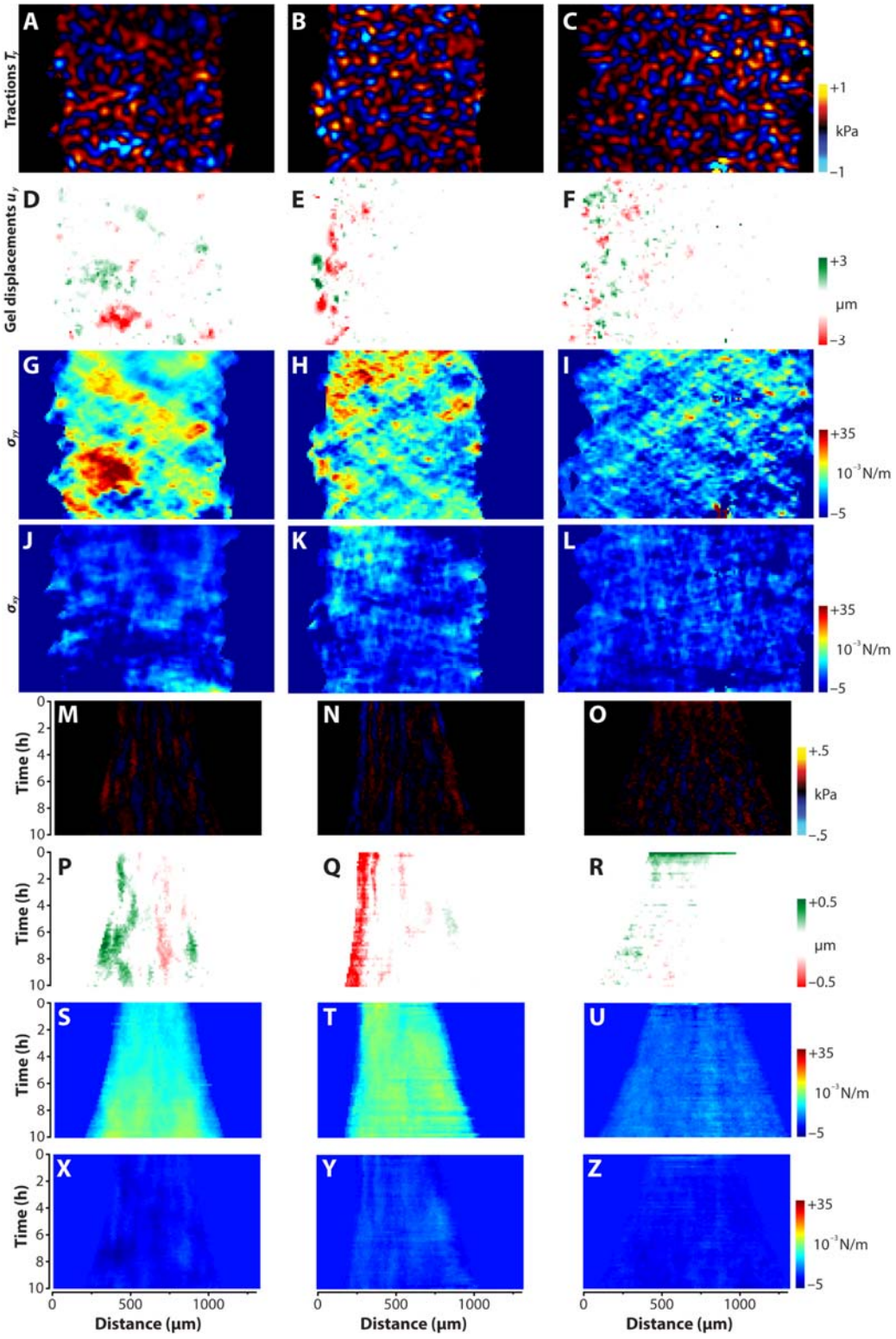

Figure S14. (A-C) Maps of the traction component T_y for the clusters depicted in Fig. 3 and Fig. S11. (D-F) Maps of the substrate displacement component u_y. (G-I) Maps of the component σ_{yy} of the 2D intercellular stress tensor. (J-L) Maps of the component σ_{xy} of the 2D intercellular stress tensor. (M-O) Kymographs of the traction component T_y. (P-R) Kymographs of the substrate displacement component u_y. (S-U) Kymographs of the 2D intercellular stress tensor component σ_{yy}. (X-Z) Kymographs of the 2D intercellular stress tensor component σ_{xy}.

Supplementary Figure S15

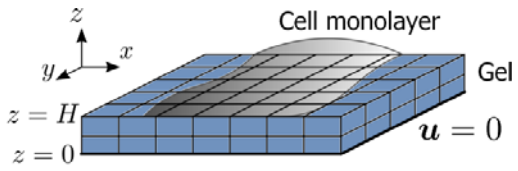

Figure S15. Example of discretization of the gel domain D in equal hexahedra using n_x =7, n_y =5, and n_z =2.

Supplementary Figure S16

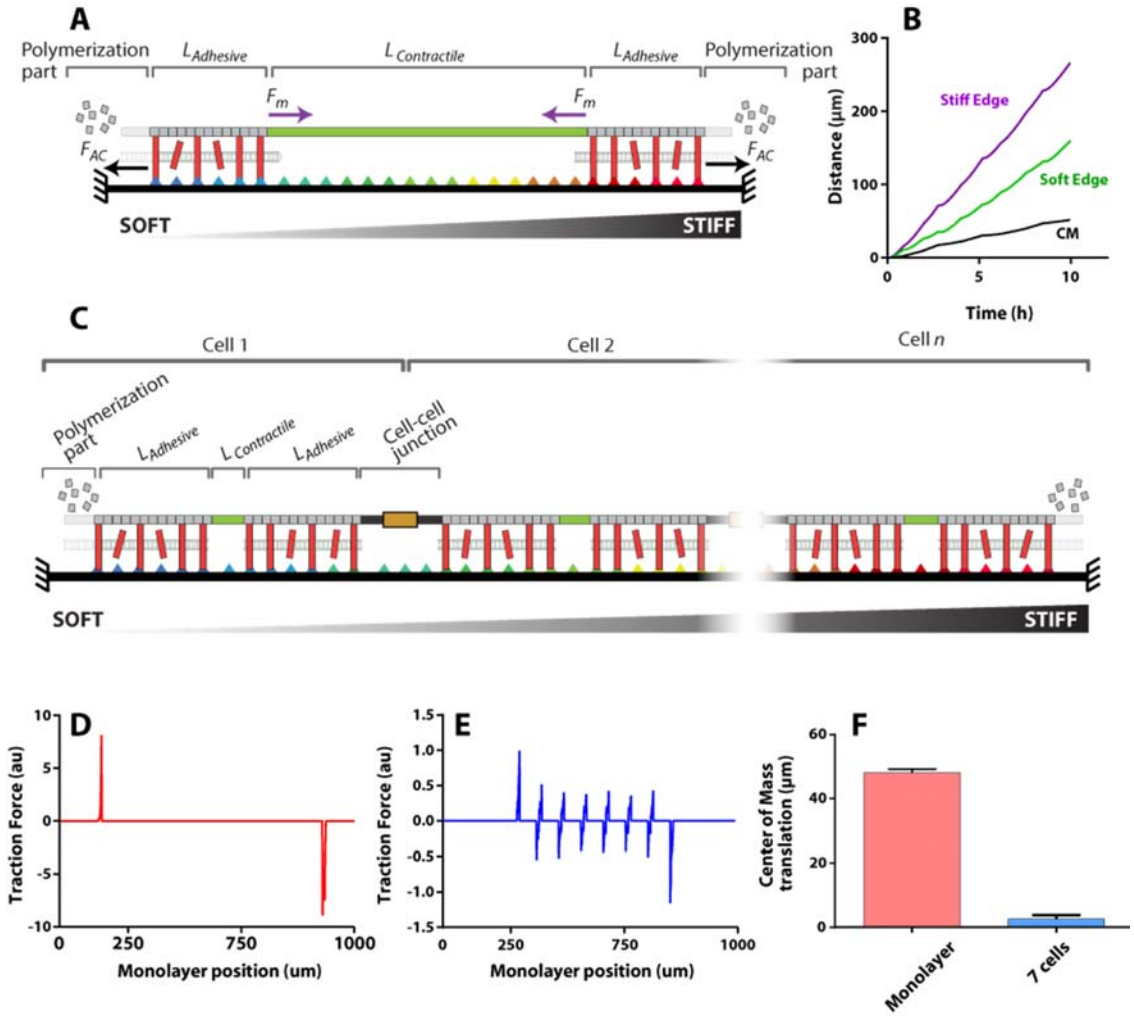

Figure S16. Scheme of the mechanical model. (A) The Monolayer part (upper horizontal bar) is connected to the substrate (lower black bar) by the adhesion complexes (ACs, red bars). The cell monolayer consists of a contractile part, an adhesive part and a polymerization part. The contractile part contracts and pulls on the rest of the monolayer with a force F_m. In the adhesive part the cell adheres to the substrate through ACs. This transmits contractile force, generating a force F_{AC} to the substrate. The polymerization part enables the monolayer to expand. (B) Example of a simulation run (steep stiffness gradient, offset 14 kPa), showing the position of the leading and trailing edges and the center of mass as a function of time. (C) Scheme corresponding to the model of a monolayer composed by several cells. Single cells are connected by cell-cell junction (orange bars). The substrate (lower black bar) is bound to the cells by the adhesion complexes (ACs, red bars). Contractile forces generated by the cells are transmitted through ACs to the substrate causing its deformation. (D) Model prediction of traction force distribution over a gradient gel generated by a single cell monolayer. The *x* axis indicates the position of the monolayer

along the substrate. The initial stiffness offset was 14kPa. (E) Model prediction of traction force distribution over a gradient gel generated by a monolayer of the same size and adhered to the same gradient gel as in D, but composed of $n = 7$ cells. The x axis indicates the position of the monolayer along the substrate. The initial stiffness offset was 14kPa. (F) Translation of the center of mass after 10 h of monolayers composed by either 1 or 7 cells.

References and notes

1. R. Majumdar, M. Sixt, C. A. Parent, New paradigms in the establishment and maintenance of gradients during directed cell migration. *Curr. Opin. Cell Biol.* **30**, 33–40 (2014).

2. P. Roca-Cusachs, R. Sunyer, X. Trepat, Mechanical guidance of cell migration: lessons from chemotaxis. *Curr. Opin. Cell Biol.*, doi:10.1016/j.ceb.2013.04.010.

3. C.-M. Lo, H.-B. Wang, M. Dembo, Y. Wang, Cell Movement Is Guided by the Rigidity of the Substrate. *Biophysj*. **79**, 144–152 (2000).

4. B. C. Isenberg, P. A. DiMilla, M. Walker, S. Kim, J. Y. Wong, Vascular Smooth Muscle Cell Durotaxis Depends on Substrate Stiffness Gradient Strength. *Biophysj*. **97**, 1313–1322 (2009).

5. M. Raab *et al.*, Crawling from soft to stiff matrix polarizes the cytoskeleton and phosphoregulates myosin-II heavy chain. *J. Cell Biol.* **199**, 669–683 (2012).

6. S. V. Plotnikov, A. M. Pasapera, B. Sabass, C. M. Waterman, Force Fluctuations within Focal Adhesions Mediate ECM-Rigidity Sensing to Guide Directed Cell Migration. *Cell*. **151**, 1513–1527 (2012).

7. T. Kawano, S. Kidoaki, Elasticity boundary conditions required for cell mechanotaxis on microelastically-patterned gels. *Biomaterials*. **32**, 2725–2733 (2011).

8. J. R. Tse, A. J. Engler, Stiffness Gradients Mimicking In Vivo Tissue Variation Regulate Mesenchymal Stem Cell Fate. *PLoS ONE*. **6**, e15978 (2011).

9. L. G. Vincent, Y. S. Choi, B. Alonso-Latorre, J. C. del Álamo, A. J. Engler, Mesenchymal stem cell durotaxis depends on substrate stiffness gradient strength. *Biotechnol. J.*, 8 (2013).

10. L. Bollmann *et al.*, Microglia mechanics: immune activation alters traction forces and durotaxis. *Front. Cell. Neurosci.* **9** (2015), doi:10.3389/fncel.2015.00363.

11. L. A. Flanagan, Y.-E. Ju, B. Marg, M. Osterfield, P. A. Janmey, Neurite branching on deformable substrates. *Neuroreport*. **13**, 2411–2415 (2002).

12. F. Liu *et al.*, Feedback amplification of fibrosis through matrix stiffening and COX-2 suppression. *J. Cell Biol.* **190**, 693–706 (2010).

13. T. A. Ulrich, E. M. de Juan Pardo, S. Kumar, The Mechanical Rigidity of the Extracellular Matrix Regulates the Structure, Motility, and Proliferation of Glioma Cells. *Cancer Res.* **69**, 4167–4174 (2009).

14. D. Cai *et al.*, Mechanical Feedback through E-Cadherin Promotes Direction Sensing during Collective Cell Migration. *Cell*. **157**, 1146–1159 (2014).

15. E. Donà *et al.*, Directional tissue migration through a self-generated chemokine gradient. *Nature*. **503**, 285–289 (2013).

16. A. Haeger, K. Wolf, M. M. Zegers, P. Friedl, Collective cell migration: guidance principles and hierarchies. *Trends Cell Biol.* **25**, 556–566 (2015).

17. A. Bianco *et al.*, Two distinct modes of guidance signalling during collective migration of border cells. *Nature*. **448**, 362–365 (2007).

18. B. A. Camley, J. Zimmermann, H. Levine, W.-J. Rappel, Emergent Collective Chemotaxis without Single-Cell Gradient Sensing. *Phys. Rev. Lett.* **116**, 098101 (2016).

19. G. Malet-Engra *et al.*, Collective Cell Motility Promotes Chemotactic Prowess and Resistance to Chemorepulsion. *Curr. Biol.* **25**, 242–250 (2015).

20. E. Theveneau *et al.*, Collective Chemotaxis Requires Contact-Dependent Cell Polarity. *Dev. Cell*. **19**, 39–53 (2010).

21. R. Sunyer, A. J. Jin, R. Nossal, D. L. Sackett, Fabrication of Hydrogels with Steep Stiffness Gradients for Studying Cell Mechanical Response. *PLoS ONE*. **7**, e46107 (2012).

22. A. Elosegui-Artola *et al.*, Rigidity sensing and adaptation through regulation of integrin types. *Nat. Mater.* **13**, 631–637 (2014).

23. D. T. Tambe, Collective cell guidance by cooperative intercellular forces. *Nat. Mater.* **10**, 469–475 (2011).

24. E. Bazellières *et al.*, Control of cell–cell forces and collective cell dynamics by the intercellular adhesome. *Nat. Cell Biol.* **17**, 409–420 (2015).

25. C. E. Chan, D. J. Odde, Traction Dynamics of Filopodia on Compliant Substrates. *Science*. **322**, 1687–1691 (2008).

26. A. Elosegui-Artola *et al.*, Mechanical regulation of a molecular clutch defines force transmission and transduction in response to matrix rigidity. *Nat. Cell Biol.* **18**, 540–548 (2016).

27. J. Escribano, M. T. Sánchez, J. M. García-Aznar, A discrete approach for modeling cell–matrix adhesions. *Comput. Part. Mech.* **1**, 117–130 (2014).

28. A. Berdahl, C. J. Torney, C. C. Ioannou, J. J. Faria, I. D. Couzin, Emergent Sensing of Complex Environments by Mobile Animal Groups. *Science*. **339**, 574–576 (2013).

29. P. M. Krafft, R. X. Hawkins, A. S. Pentland, N. D. Goodman, J. B. Tenenbaum, in *Proceedings of the 37th Conference of the Cognitive Science Society* (Cognitive Science Society, 2015).

30. J. Alcaraz *et al.*, Microrheology of Human Lung Epithelial Cells Measured by Atomic Force Microscopy. *Biophysj*. **84**, 2071–2079 (2003).

31. M. Dembo, Y. L. Wang, Stresses at the cell-to-substrate interface during locomotion of fibroblasts. *Biophys. J.* **76**, 2307–2316 (1999).

32. J. J. Muñoz, Non-regularised Inverse Finite Element Analysis for 3D Traction Force Microscopy. *Int. J. Numer. Anal. Model.* (2016).

33. C. Selhuber-Unkel *et al.*, Cell adhesion strength is controlled by intermolecular spacing of adhesion receptors. *Biophys. J.* **98**, 543–51 (2010).

34. T. Kim, W. Hwang, R. D. Kamm, Computational Analysis of a Cross-linked Actin-like Network. *Exp. Mech.* **49**, 91–104 (2007).

35. J. Escribano, M. T. Sánchez, J. M. García-Aznar, Modeling the formation of cell-matrix adhesions on a single 3D matrix fiber. *J. Theor. Biol.* **384**, 84–94 (2015).

36. E. A. Novikova, C. Storm, Contractile Fibers and Catch-Bond Clusters: a Biological Force Sensor? *Biophys. J.* **105**, 1336–1345 (2013).

37. F. Kong, A. J. García, A. P. Mould, M. J. Humphries, C. Zhu, Demonstration of catch bonds between an integrin and its ligand. *J. Cell Biol.* **185**, 1275–1284 (2009).

38. M. L. Gardel *et al.*, Traction stress in focal adhesions correlates biphasically with actin retrograde flow speed. *J. Cell Biol.* **183**, 999–1005 (2008).

39. N. Wang, Mechanical Interactions Among Cytoskeletal Filaments. *Hypertension*. **32**, 162–165 (1998).

40. P. Roca-Cusachs, T. Iskratsch, M. P. Sheetz, Finding the weakest link – exploring integrin-mediated mechanical molecular pathways. *J. Cell Sci.* **125**, 3025–3038 (2012).

41. I. Acerbi *et al.*, Human breast cancer invasion and aggression correlates with ECM stiffening and immune cell infiltration. *Integr. Biol. Quant. Biosci. Nano Macro*. **7**, 1120–1134 (2015).

42. C. Storm, J. J. Pastore, F. C. MacKintosh, T. C. Lubensky, P. A. Janmey, Nonlinear elasticity in biological gels. *Nat. Cell Biol.* **435**, 191–194 (2005).

43. J. H. Wen *et al.*, Interplay of matrix stiffness and protein tethering in stem cell differentiation. *Nat. Mater.* **13**, 979–987 (2014).